On the interaction of internal tides over two adjacent sills in a fjord

Jiuxing Xing[1] and Alan M. Davies[1]

Received 13 April 2010; revised 15 December 2010; accepted 1 February 2011; published 22 April 2011.

[1] The problem of to what extent two topographic features, namely, adjacent sills in a fjord, interact to modify the internal waves between the sills is considered using a two-dimensional vertical slice nonhydrostatic model. Motion is generated by forcing with a barotropic tide at the M_2 frequency. Calculations are performed with a range of sill depths h_s and sill separations L. Initially, a single sill is considered and a progressive internal tide, lee waves, and a baroclinic jet are formed in the region of the sill. When a second sill is introduced, the intensity of the sill jet is reduced and a standing internal tide is generated between the sills, with an associated increase in mixing and change in tidal energy flux. However, as the sill separation increases, the energy flux increases toward its single sill value. For higher harmonics of the tide, which have a wavelength shorter than the intersill separation, their magnitude is increased for certain sill separations L due to focusing with an associated broadband resonance. In essence, nonlinear interaction of waves between the sills increases mixing, which explains the observed enhanced mixing found in observations made in such regions.

Citation: Xing, J., and A. M. Davies (2011), On the interaction of internal tides over two adjacent sills in a fjord, *J. Geophys. Res.*, *116*, C04022, doi:10.1029/2010JC006333.

1. Introduction

[2] Although the generation of propagating internal tides, their nonlinear interaction, and the associated short waves, in shelf edge regions [e.g., *Holt and Thorpe*, 1997] and the resulting mixing due to internal waves [*Van Haren et al.*, 2002; *Van Haren*, 2004] has been a research topic for many years [see, e.g., *Pingree and New*, 1989, 1991; *Lamb*, 1994; *Vlasenko et al.*, 2005], little work has been done to examine how internal tides generated at two topographic features interact with one another and the associated mixing. The recent notable exception here is the work of *Chao et al.* [2007], who examined internal tide generation over two ridges in the Luzon Strait. The classic picture of internal tide generation at the shelf edge (or any steep isolated topographic feature, e.g., seamount, ridge, or sill) is that of an on-shelf/off-shelf barotropic tide giving rise to a vertical displacement of the pycnocline, which, as it moves over the shelf slope, gives rise to a progressive internal wave (internal tide) (see, e.g., *Baines* [1995], *Legg* [2004a, 2004b], *Legg and Klymak* [2008], and classic sill observations of *Farmer and Armi* [1999a, 1999b] and *Farmer and Dugan* [1980]). Depending upon the ratio of the local topographic slope s = dh/dx (with h water depth and x across-shelf coordinate) to the internal wave slope given by $\alpha = ((\omega^2 - f^2)/(N^2 - \omega^2))^{1/2}$, where ω is tidal frequency, f is Coriolis frequency, and N is local buoyancy frequency, the tide is classed as subcritical ($s/\alpha < 1$), critical ($s/\alpha = 1$), or supercritical ($s/\alpha > 1$). Maximum internal tide generation occurs at the critical slope, and depending upon shelf slope topography, internal wave propagation onto the shelf or back into the ocean along raypaths can occur. In the case of an oceanic propagating internal tide, it can be reflected by off-shelf topography such as a seamount, thereby changing the spatial distribution in the shelf edge region [*Xing and Davies*, 1998] compared to that at other locations where there is no seamount. Associated with the reflection and interaction of internal tidal beams are regions of enhanced mixing [e.g., *Eriksen*, 1985]. This problem has been examined in the context of interaction of internal tides in an off-shelf region, namely, the Anton Dohrn seamount and the shelf edge off the west coast of Scotland by *Xing and Davies* [1998]. In addition, the importance of small-scale topography on the shelf slope upon internal tide generation was examined by *Legg* [2004a, 2004b] and *Thorpe* [2001].

[3] Besides understanding the influence of small-scale topography in shelf edge regions upon local mixing being an important topic in its own right, recent research [*Samelson*, 1998; *Spall*, 2001; *Saenko*, 2006] has shown that it has major implications in climate models. However, a major difficulty with examining how internal tidal waves from two topographic features interact in a shelf edge environment is the three-dimensional nature of the problem [*Cummins and Oey*, 1997] and the complexity of making detailed measurements of tidal energy flux and mixing in such a complex open-ocean environment (e.g., the Hawaiian Islands [*Carter et al.*, 2008]).

[4] In the case of internal tide generation in tidally forced fjords or lochs [e.g., *Vlasenko et al.*, 2002; *Inall et al.*, 2004, 2005], the problem is essentially two-dimensional in the x-z plane, with x the along-fjord axis and z the vertical coordinate. As such, more detailed measurements can be

[1]National Oceanography Centre, Liverpool, UK.

0148-0227/11/2010JC006333

made, and also idealized process type models can be used to understand the mechanisms leading to internal tide generation, reflection, interaction, and the associated change in the Richardson number distribution, which has implications for mixing.

[5] Although internal tide generation, propagation, and interaction has been studied in shelf edge and oceanic situations, to the authors' knowledge no modeling work of this type has been performed in fjord and loch regions containing two sills. As will be shown here, the presence of two sills can give rise to internal wave reflection, leading to a standing internal tide between the two sills, which is analogous to the standing internal wave (seiche motion) induced in a stratified lake by wind forcing [*Hall and Davies*, 2005]. Although standing internal tides have been observed in lochs, between the sill at the entrance to the loch and its head [e.g., *Allen and Simpson*, 1998], and within a canyon [*Petruncio et al.*, 1998], to the authors' knowledge no study, other than a preliminary calculation of *Xing and Davies* [2009] for a single sill separation, has been made of how multiple sills within fjords and lochs can produce standing internal tides. In addition, how sill separation influences this interaction, the role of higher harmonic resonance, the associated Richardson number distribution, mixing, and internal wave energy flux have not been considered.

[6] In this paper the mechanisms giving rise to internal tide generation, interaction, energy flux, and Richardson number distribution in a tidal fjord with two symmetric shallow sills are examined. Initially, the influence of sill depth and tidal forcing for a single shallow sill are briefly considered and related to recent work of *Legg and Klymak* [2008, hereinafter LK08] and *Klymak et al.* [2010, hereinafter K10], who considered a large parameter space for a single obstacle in deep water. The difference in response, compared to a deep-water obstacle, in the shallow single-sill case, namely, the change between wave and jet response, is highlighted, as this is a distinct difference between sill (in shallow water) and ridge (in deep water). Subsequently, the two-sill case (the main focus of the paper) is considered. In this case, again the influence of sill depth and tidal forcing are briefly examined, but the role of sill separation upon the internal tide and associated mixing are examined in more detail. These calculations are performed in the context of a typical two-sill tidal fjord, such as the Ringdals Fjord–Idefjord at the Swedish-Norwegian border, where detailed measurements were recently made showing enhanced mixing and dissipation between the sills [*Johnsson et al.*, 2007]. This enhanced level of mixing was interpreted in terms of that due to a progressive internal tide generated at a single sill. *Johnsson et al.* [2007] attempted to account for both sills by considering each sill independently in turn and linearly combining solutions, thereby assuming there was no interaction between the two sills. Here it is shown for short sill separation that the presence of a second sill can give rise to a standing internal tide between the sills with an associated increase in mixing due to this process. Hence there can be interaction between internal waves generated at each sill. In addition, as the sill separation increases the solution approaches that of an isolated sill, and then there is no interaction. However, since higher harmonics of the M_2 internal tide are generated at each sill, and for some of these harmonics the intersill separation is comparable to their wavelength, then focusing and resonance can lead to increased amplitude and hence enhanced interaction at specific intersill separations. Therefore the interaction between the sills does not simply reduce with their separation but is modified by focusing and resonance. For typical intersill separations in fjords, of order 10 km, and shallow water depths, about 100 m and typical vertical density profiles [*Johnsson et al.*, 2007], as will be shown, this resonance primarily occurs at the higher harmonics of the M_2 tide, namely, the short waves that are responsible for mixing. The model used in the calculations together with the domain of interest are presented in section 2. In sections 3 and 4 a range of calculations with varying parameters that control the internal tide and mixing are discussed. In section 5, results of the calculations are summarized.

2. Model

[7] Following the successful use of the nonhydrostatic MIT-gcm code [*Marshall et al.*, 1997] to model internal tides in deep (depths of over 1000 m) ocean regions [e.g., *Legg*, 2004a, 2004b; *Legg and Huijts*, 2006] and their generation over shallow sills [*Xing and Davies*, 2006, 2007, hereinafter XD06 and XD07], the same code is used here. As extensive details are given in the literature, they will not be repeated. The model uses a z coordinate in the vertical with "shaved cells" in the near-bed region to take account of variations in bottom topography. An alternative approach is to use a sigma coordinate in the vertical as applied by *Berntsen and Furnes* [2005] and *Berntsen et al.* [2006] in their nonhydrostatic model. However, as shown by *Berntsen et al.* [2006], both approaches yielded solutions that were not significantly different.

[8] Resume In the present process-oriented study, two symmetric identical idealized sills are considered, with the first sill placed at x = 0 and the second a distance L to its right. The use of two symmetric sills is consistent with the topography of the region where measurements were made by *Johnsson et al.* [2007]. Calculations are performed initially with a single sill at x = 0 (Figure 1a), and subsequently with two sills for a range of intersill separations L extending to 10 km (Figure 1b), a typical sill separation in a fjord. The sill's shape is given by

$$h_0 \Big/ \left(1 + \left(\frac{x}{\lambda}\right)^4\right),$$

with h_o sill height and the parameter λ = 125 m giving a sill half width a_o of order 500 m. The channel is open at both ends and extends to x = ±150 km, although only a subdomain is shown in Figures 1a and 1b. By using this length of channel, any small false reflection of the internal wave at the open boundaries (where a sponge condition is applied) does not propagate back to the region of the sills within the integration period. Previous single sill calculations with a range of resolutions [*Berntsen et al.*, 2008] showed that an accurate solution could be obtained with fine vertical (dz = 1 m) and horizontal (dx varied smoothly from 10 m at the sills to 800 m elsewhere) grids. In the series of calculations presented later, initially the sill height h_o, and hence aspect ratio a_o/h_o, together with sill depth h_s, were chosen to represent those in a typical fjord. In order to examine how

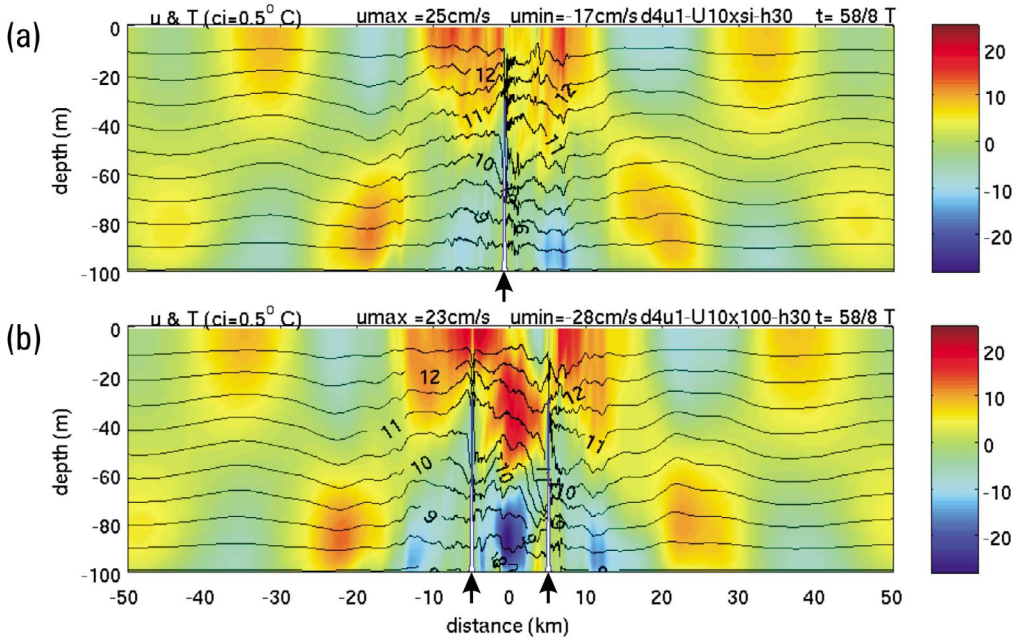

Figure 1. (a) Subdomain of the sill region, i.e., x = −50 km to 50 km, showing a single sill at x = 0, temperature field (°C, contour interval (c.i.) = 0.5°), and the u velocity (cm s^{-1}) at t = 58/8T (with T the tidal period) and (b) two sills with L = 10 km. Sill positions are shown by the arrow.

the presence of a second sill influences the internal tide generated at a single sill, calculations were performed with both one and two sills for this choice of sill parameters, for a fixed intersill separation L. However, as shown by *Baines* [1995] and others [e.g., XD06; XD07; *Berntsen et al.*, 2006, 2008], the choice of sill parameters does influence internal tide generation, at a single sill. As the single sill case has been investigated for a large range of parameters, here only a small number of these parameters are considered to check that the conclusions concerning the presence of the second sill are valid in the more general case. In addition for oceanic depths (of order 2000 m) a detailed parameter study has been performed by LK08 for tidal flow and by KL10 for steady flow. Results from LK08 are used to understand the single sill calculations and extend their range. In addition, the shallow single sill calculation is used to illustrate the formation of a jet on the downstream side of the sill, which does not occur in the deep oceanic case of LK08. However, since the focus here is how the presence of the second sill influences the internal tide and mixing in the intersill region, a more extensive set of calculations are subsequently performed with fixed sill parameters but varying the distance L.

[9] Motion in the region was started from a state of rest, with horizontal temperature surfaces and barotropic tidal forcing of amplitude U_o applied as a body force. Outside the sill regions this gave rise to tidal velocities of corresponding amplitudes, although in the region of the sill (see section 3) the barotropic current increased as water depth decreased. If the rigid lid approximation was used, then the ratio of barotropic current speed to local water depth would be constant. However, in the present case the model has a free surface, and hence this ratio changes with space and time. By varying U_o, the sensitivity of the solution to changes in across-sill velocity U_s could be briefly determined, with results from LK08 used to interpret this response and extend it to other parameter spaces. In all initial calculations (Table 1), forcing was at the M_2 tidal period ω, with Coriolis frequency $f = 1.2 \times 10^{-4} s^{-1}$ and initial buoyancy frequency $N = 0.01 s^{-1}$. Although the same initial value of N is used everywhere, its distribution changes with time as mixing occurs. These parameters have been used previously in single sill calculations (XD06; XD07) and are appropriate here.

[10] As fine numerical grids were used in the calculations and a nonhydrostatic model was applied, then small-scale mixing could be approximated with minimum values of vertical (K_V) and horizontal (K_h) diffusivities, i.e., $K_V = K_h = 10^{-7}$ m^2 s^{-1}. Consequently, mixing was controlled by small-scale processes, namely, shear instabilities and overturning that were generated in the nonhydrostatic model and could be resolved on the fine grid. To maintain numerical stability without artificially damping the solution [*Berntsen et al.*, 2008], background eddy viscosity values, namely, $A_V = 10^{-3}$ m^2 s^{-1} and $A_h = 10^{-1}$ m^2 s^{-1}, were used together with a time step of 2 s. Ideally a significantly finer grid than that used here, with smaller values of these parameters, in

Table 1. Summary of Parameters Used in the Calculations With M_2 Tidal Forcing

Calc	Forcing Velocity U_o (m s^{-1})	Sill Depth h_s (m)	Single (S) or Double (D) Sill	Sill Separation L (km)
1	0.1	30	S	…
2	0.1	30	D	1.5
3	0.1	15	D	1.5
4	0.05	15	D	1.5
5	0.1	60	D	1.5
6	0.1	30	D	2.5
7	0.1	30	D	5.0
8	0.1	30	D	10.0

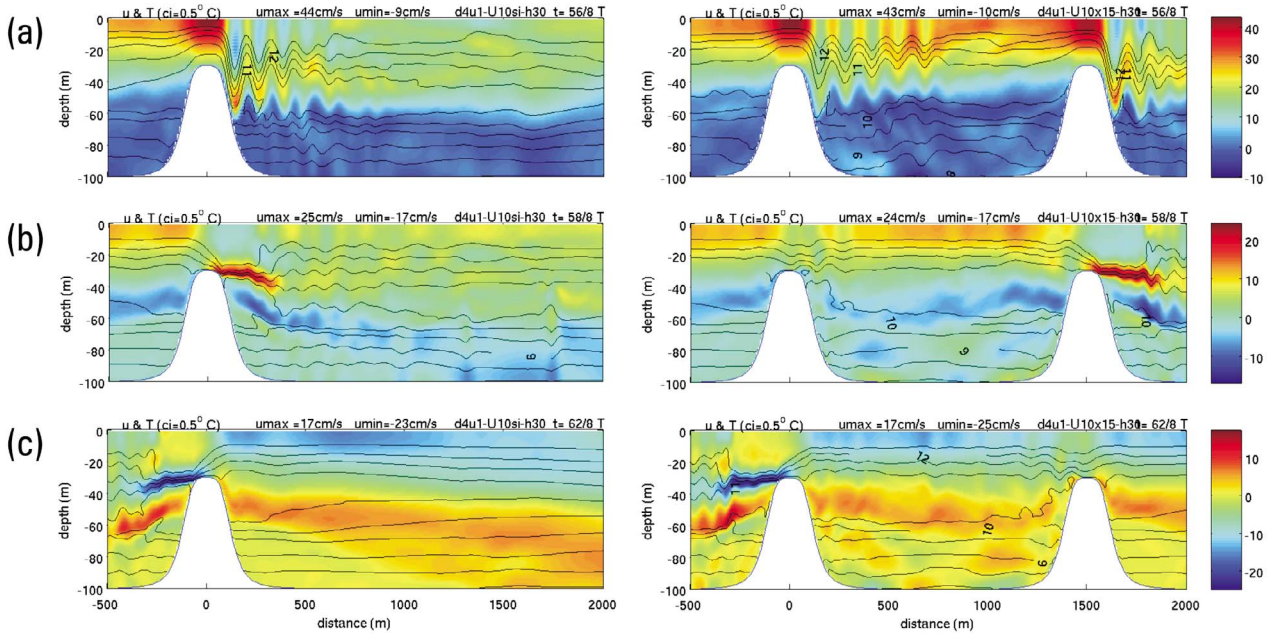

Figure 2. Subdomain of the sill region, i.e., x = −500 m to 2000 m, for (left) a single sill with h_s = 30 m, showing velocity u (cm s^{-1}) and temperature field (°C, c.i. = 0.5°) at (a) t = 56/8T, (b) t = 58/8T, (c) t = 62/8T, and also (right) two sills separated by L = 1.5 km.

particular, an A_V value comparable to the K_V value could be used. However, as shown by *Berntsen et al.* [2008], as A_V and A_h values are reduced, small-scale eddies that cannot be resolved without an extremely fine grid (that is computationally prohibitive) are generated, grow, and eventually destabilize the solution. However, without an extremely fine grid, an accurate determination of the mixing is not possible. Rather, the approach followed here is that adopted by *Legg* [2004a, 2004b] and *Legg and Huijts* [2006] of examining Richardson number distributions and changes in the buoyancy anomaly, namely, to examine how changes in sill topography and intersill separation influence the distribution of the Richardson number. In addition, the change in the temperature field due to parameter variations in particular intersill separation will be quantified in terms of changes in buoyancy frequency N. Despite the fine grid applied in the model and low values of sub-grid-scale mixing, there is some artificial damping and diffusion associated with the numerical techniques, in particular, the advection scheme (which is second order with the application of flux limiter) used in the model. This presents a difficulty in comparing modeled and observed mixing [see *Burchard and Rennau*, 2008; *Rennau and Burchard*, 2009] but is less of a problem in examining how intersill separation influences the solution. However, as shown by *Vlasenko et al.* [2005], it can artificially widen and damp tidal beams that will influence focusing and resonance (see section 5). Approaches aimed at reducing artificial numerical damping and mixing [*Klymak and Legg*, 2010] will help to reduce this problem.

[11] In order to quantify the interaction between the two sills, it is interesting to see how the presence of the second sill influences mixing in the sill region, the energy flux magnitude, and distribution compared to a single sill. Owing to dissipation and mixing, which are shown by *Johnsson et al.* [2007] to be very large in these fjord systems, energy is removed from the internal tide as it propagates away from its generation point. Consequently, as the separation distance L increases, then the solution in the intersill region should converge to that of a single sill, as the influence of the second sill is reduced. However, as will be shown, for typical intersill separations in fjords this picture is complicated by focusing and resonance at higher harmonic frequencies. As shown by *Davies et al.* [2009], in the case of a steep sill in shallow water it is essential to retain both the nonlinear and free surface terms in the energy flux calculation. As details of energy flux calculations are given by *Venayagamoorthy and Fringer* [2005] and *Moum et al.* [2007], they will not be presented here.

3. Single- and Two-Sill Calculations With L Fixed

[12] In order to quantify and understand how the presence of the second sill influences the solution in the region between the sills, it is essential to initially briefly examine a single-sill solution. This is done in the context of the detailed study of LK08 who examined the response of a tall steep ridge to tidal flow in oceanic depths. Here difference between the shallow sill and deep oceanic problem are stressed.

3.1. Single-Sill Calculation (Calc 1), U_o = 0.1 m s^{-1}, h_s = 30 m

[13] In an initial calculation (Table 1), forcing was at the M_2 frequency and U_o was fixed at 0.1 m s^{-1}, with sill depth h_s = 30 m and sill half width a_s = 500 m. As a detailed study of the response of a shallow single sill to a range of U_o, a_s and h_s values is given by XD06, and for the deep oceanic case by LK08, only the main features that are relevant to the two-sill calculations will be presented here. As shown by

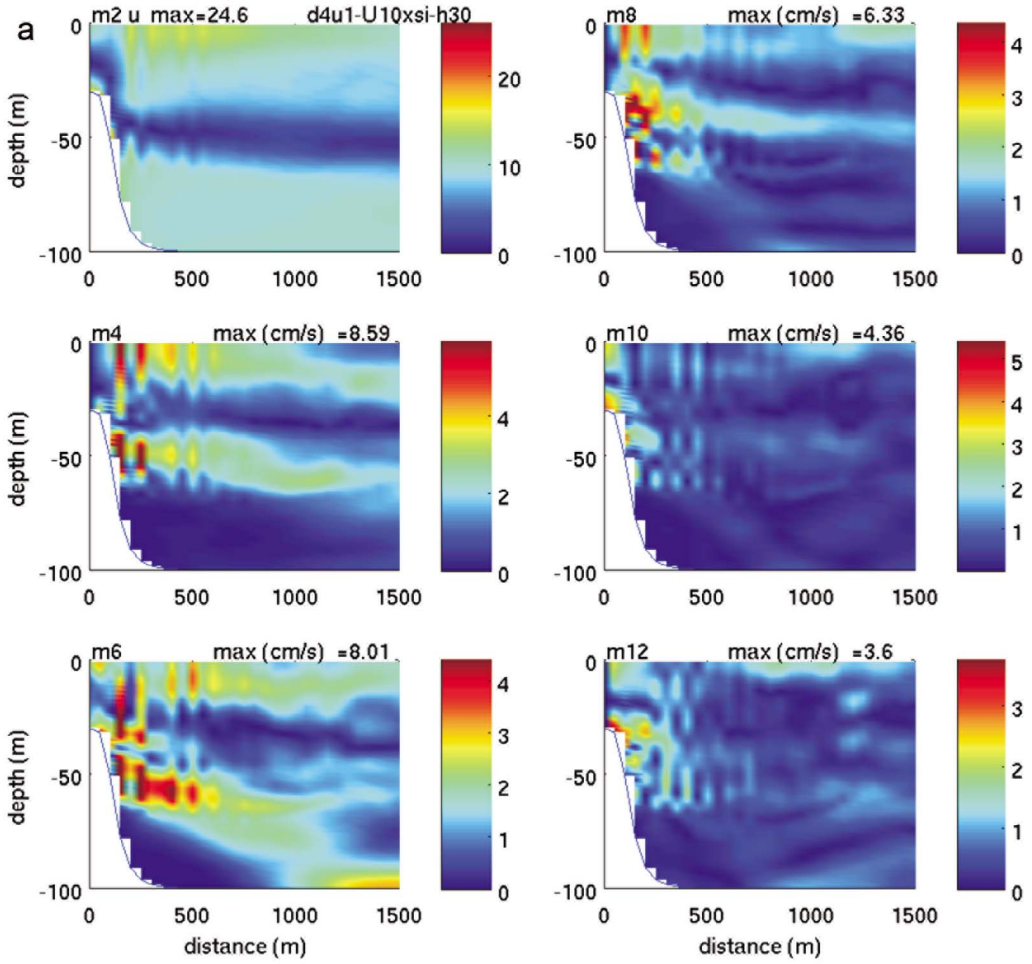

Figure 3. (a) Subdomain of the sill region showing amplitude (cm s^{-1}) of the u component of the baroclinic velocity for the M_2, M_4, M_6, M_8, M_{10}, and M_{12} tidal constituents, for a single sill with h_s = 30 m. (b) As in Figure 3a but for phase (degrees). (c) As in Figure 3a but for contours of the amplitude of the vertical velocity w (cm s^{-1}) (c.i. = 0.1).

LK08, higher harmonics of the M_2 tide are generated when $U_0/(\omega a_s) > 1$, which is certainly true in this case and later examined in detail. In addition, the parameter U/N where U is taken as U_0 or the across sill velocity determines the amplitude of lee wave generation (LK08), which as shown by XD06, is appreciable in this case.

[14] As the objective of the present paper is to determine how internal tide generation, energy flux, and associated change in Richardson number and mixing are influenced by the presence of a second topographic feature, in our case the sill to the right of the first sill (Figure 1b), then in general only the region to the right of the single sill will be examined in detail (Figure 2). However, initially the 50 km domain on either side of the sill will be briefly considered to determine the spatial variability of the tide outside the region between the sills. In order to establish a near periodic tide the model was "spun up" for seven tidal cycles, namely, to t = 7T with T the tidal period. The physical nature of the internal tide generated over topography is that it propagates away from its generation point along beams on both sides of the sill and is subsequently reflected at the sea surface and seabed as it propagates away from its generation region (Figure 1a). This gives rise to regions of enhanced and reduced u current (Figure 1a) with a phase shift of 180° between surface and bottom currents, and a horizontal wavelength λ_h of about 27 km. The vertical phase shift of 180° indicates a first mode internal tide, with wavelength $\lambda_z = 2h$, with h water depth. These values are in agreement with those computed from the dispersion relation with ω the M_2 tidal frequency, namely, the internal wave slope α is given by

$$\alpha = \frac{\lambda_z}{\lambda_h} = \left(\frac{\omega^2 - f^2}{N^2 - \omega^2}\right)^{1/2}. \quad (1)$$

Consequently, the solution is dominated by the first mode M_2 internal tide, the horizontal wavelength of which exceeds the typical intersill separation considered here of up to L = 10 km (see section 5). However, for the higher harmonics of the tide their horizontal wavelengths are significantly smaller (see section 5) and can lie below this. It is evident from Figure 1a that associated with this internal tide in the region away from the topography there are vertical displacement of the density surfaces produced by the

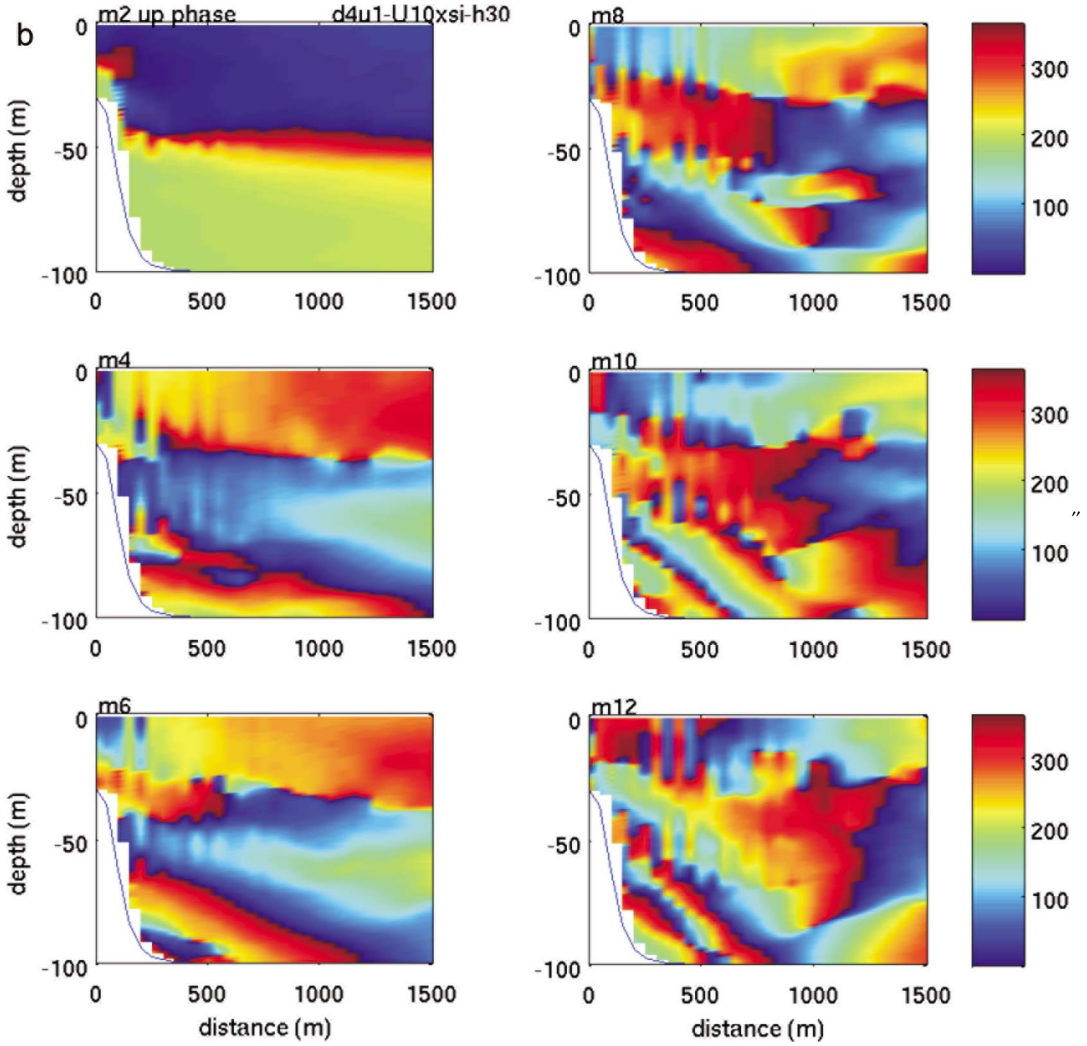

Figure 3. (continued)

internal tide. However, in the region of the sill topography (up to about 10 km either side of it) there are significant short wave displacements associated with lee waves, as predicted by LK08 for steep topography (i.e., dh/dx > ω/N), the case here, and with an amplitude that scales as U/N. In addition, solitons are generated at the sill. In essence, as the barotropic tide flows over the sill, the density field is displaced and an internal tide is generated which propagates along internal tidal beams away from the sill [*Vlasenko et al.*, 2005]. In addition, during flood tide unsteady lee waves (wavelengths of order 100 m) and mixed tidal-lee waves [*Nakamura et al.*, 2000; *Nakamura and Awaji*, 2001] are generated on the lee side of the sill. These waves are responsible for the small-scale displacement of the thermocline contours shown in Figures 1a and 2 up to 1000 m downstream of the sill. Associated with the generation of internal lee waves and tidal waves, there is significant mixing in the region of sills. To see how the internal waves and associated mixing are modified by the presence of a second sill, it is necessary to examine the near-sill region in detail and within a tidal cycle. For this region a "snapshot" of the solution was saved at every 1/8T (Figure 2).

[15] Consider the near-sill region, in particular, the area between x = 0 and 2000 m, namely, the region which in the two sill case lies between the sills. It is evident in the single-sill calculation (Figure 2a, t = 56/8T) that at the end of the seventh tidal cycle when the baroclinic tide is fully developed and the across-sill flow is near maximum, that lee waves are present on the downstream side of the sill, as shown by the small-scale (of order 100 m) displacements of the isotherms. In addition to the unsteady lee waves, a jet separates from the sill, leading to an increase in midwater tidal velocity downstream of the sill. This jet is associated with the high tidal flow over the sill and is characteristic of sill flows which for the parameters used here exhibit a mixed jet and wave like response (XD06) rather than the wavelike response found in the deep ocean (LK08). Associated with this jet and the lee waves is an increase in midwater mixing in the region of the sill. As time progresses, the intensity of the jet increases, and at t = 58/8T an

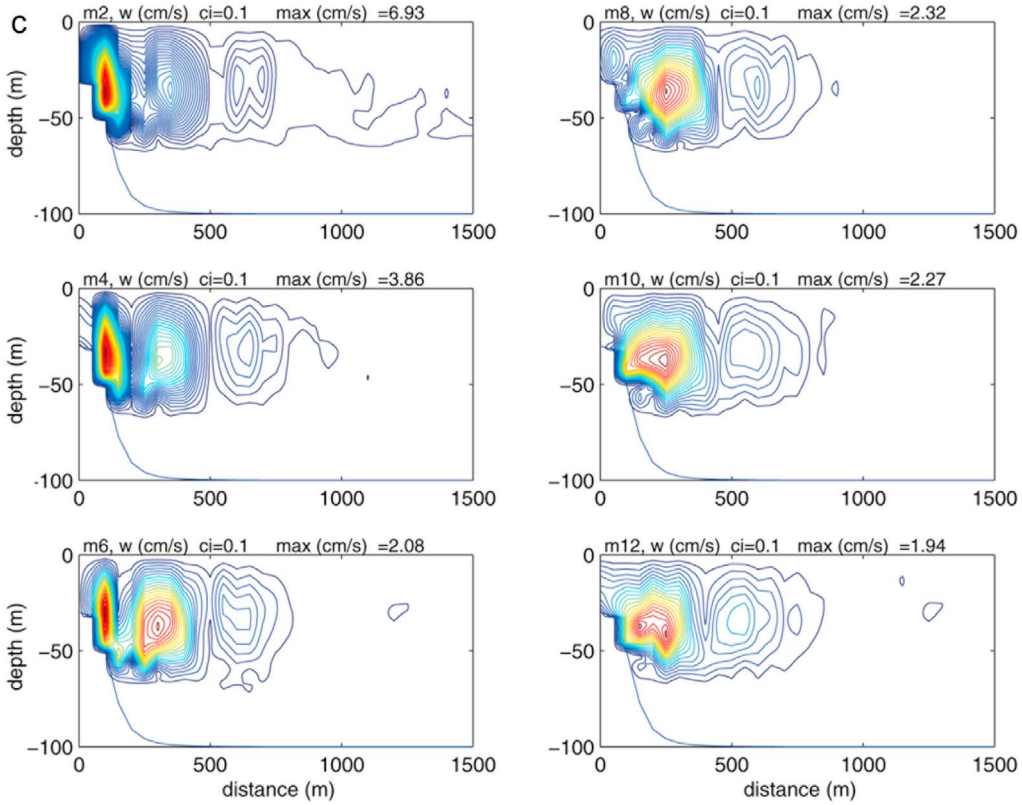

Figure 3. (continued)

intense jet has separated from the top of the sill (Figure 2b). As the tidal flow reverses, lee waves are formed on the left-hand side of the sill (not presented). At t = 62/8T (namely, half a tidal cycle following Figure 2b (t = 58/8T)) a corresponding jet, although with current in the opposite direction, has formed on the left-hand side of the sill (Figure 2c). As discussed by *Johnsson et al.* [2007] and found here, the internal response of the sill flow varies between internal wave generation (found at t = 56/8T) and jet (found at t = 58/8T and 62/8T) depending upon flow over the sill.

[16] To examine the spatial distribution of the internal tide at both the fundamental frequency and its higher harmonics and how this is subsequently influenced by the presence of a second sill (see section 3.2), a harmonic analysis of the u-component of the baroclinic velocity on the right-hand side of the sill was performed (Figures 3a and 3b). Only output at every fifth model grid point was used in this harmonic analysis. This is the reason why the topography of the sill appears to be poorly represented in Figure 3a. In reality, with Δz = 1 m and Δx = 10 m as used in the model, together with the shaved cell approach, the topography is accurately reproduced in the model. Figures 3a and 3b shows for the M_2 component a region of surface intensified amplitude (of up to 15 cm s^{-1}) with decreasing surface amplitude with distance downstream of the sill. At about midwater the tidal amplitude is near zero, with a slight increase at depth. The phase plot (Figure 3b) reveals a 180° phase change in the vertical, showing the presence of a first mode baroclinic internal tide. This is consistent with the "far-field" distribution of the internal tide shown in Figure 1a. Small-scale spatial variations in the amplitude and phase of the M_2 component of the tide are evident in the near-sill region in both Figures 1a and 3a and are due to some mixing occurring in the near-sill region. Since this mixing is associated with the lee waves and the jet, then the buoyancy frequency will vary with space and time. A consequence of this is that the raypaths will broaden and become less distinct in the near-sill region. This is a very different situation than in the deep ocean (water depths of order or exceeding 1000 m and barotropic tidal velocities of order 10 cm s^{-1}) where tidal velocity and mixing are appreciably less and raypaths are well defined [*Legg and Huijts*, 2006]. In essence, more well defined raypaths are evident in Figure 1a, in the regions away from the sill where the mixing is reduced.

[17] For the M_4 component, regions of surface intensification are present, with corresponding local intensification (amplitude up to 8 cm s^{-1}) at about middepth, suggesting that a higher vertical mode is formed closer to the sill. This is supported by the phase change which varies rapidly through the vertical (Figure 3b). For the M_6 and higher harmonics it is evident that there is some surface and mid-water increase in amplitude, although the horizontal spatial variability increases rapidly due to their shorter wavelength. In addition, the phase distribution of these higher harmonics shows significant changes in the horizontal and vertical due to their shorter wavelength and the presence of higher modes. Some weak beam-like structures are evident in these higher modes. From simple theory, the slope α of the raypaths of the various harmonics can be computed using the formula given earlier, with N set at its initial value and ω corresponding to the M_2 to M_{12} frequency. This gives slopes of 0.8%, 2.6%, 4.2%, 5.5%, 7.0%, and 8.4% for the M_2 to

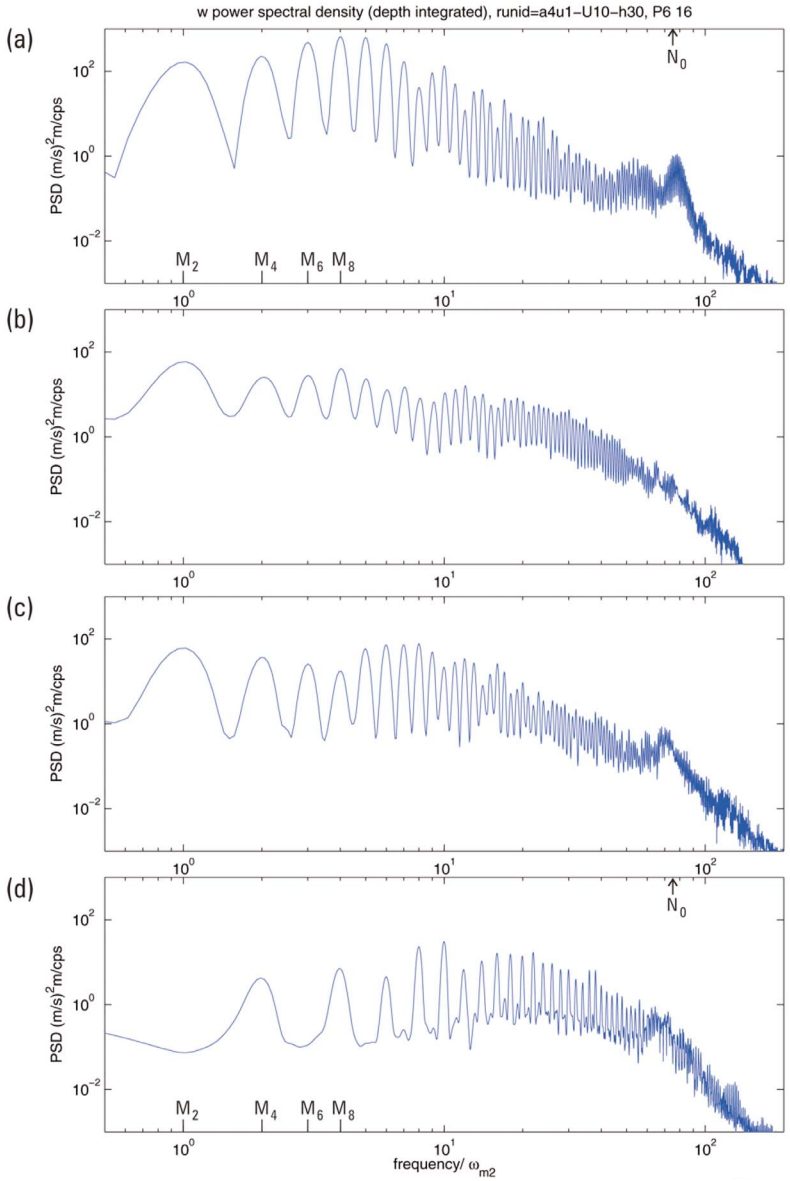

Figure 4. Power spectra of the vertical velocity, integrated through depth, normalized with respect to the M_2 tide at (a) x = 250 m and (b) x = 750 m in the single-sill case. Also shown (c and d) are power spectra (at x = 250 m and 750 m, respectively) in the double-sill case for L = 1.5 km. Tidal frequencies M_2, M_4, M_6, and M_8 and initial buoyancy frequency N_0 are marked with arrows.

M_{12} constituents. In practice, however, the mixing in the sill region (XD06) leads to a broadening of these raypaths, which are less distinct than in the deep ocean [*Legg and Huijts*, 2006] where mixing is a minimum. In addition, close to the sill region enhanced mixing changes the generation point for the various harmonics which together with wave-wave interaction modifies their spatial distribution from that given by simple ray theory. It is evident from the amplitude and phase distributions given in Figures 3a and 3b that the higher harmonics have significantly shorter horizontal and vertical wavelengths than the M_2 tide.

[18] Contours of the amplitude of the vertical velocity (Figure 3c) for the M_2, M_4, and M_6 constituents reveal a maximum at about z = −40 m close to the sill, with other weaker maxima occurring some distance away from the sill. This suggests that the internal tide is generated close to the top of the sill but decays with distance away from its generation point. This decay is more rapid than that found in the deep (depths exceeding 1000 m) ocean [*Lamb*, 2004; *Legg and Huijts*, 2006] and is associated with the higher mixing in shallow regions due to increased barotropic tide, reduced water depth, and, particularly in the sill region as discussed previously, internal mixing due to lee waves and the jet that separates from the sill. For the other higher harmonics, the region of maximum vertical velocity is slightly farther away from the sill. This spatial variability in the vertical velocity distribution reflects the spatial variability found in the u current amplitude (Figure 3a). It is clear from Figure 3c

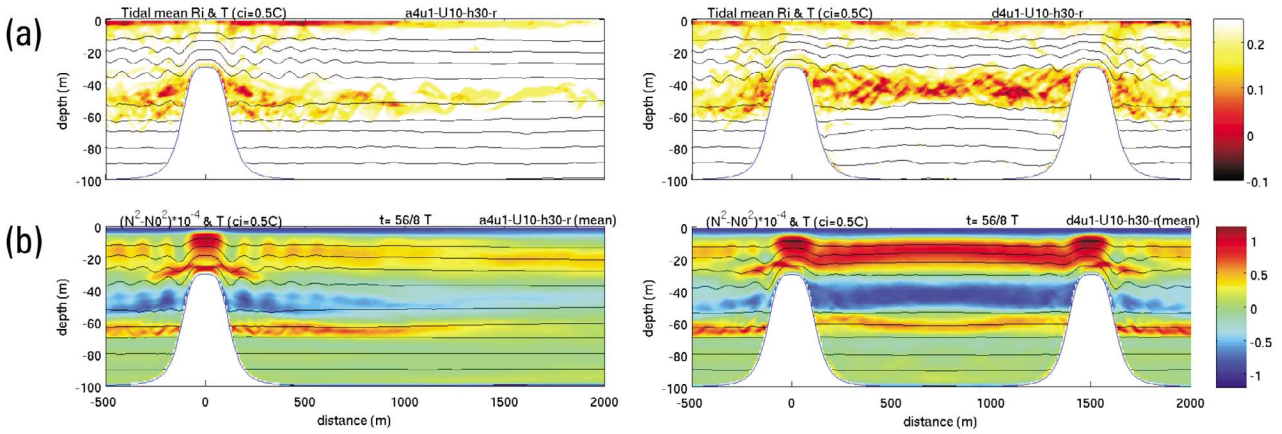

Figure 5. Subdomain of the sill region for the (left) single and (right) double sill cases, showing the tidally averaged temperature field (°C, c.i. = 0.5°) together with (a) the tidally averaged Richardson number and (b) the tidally averaged change in buoyancy frequency, $DN = (\overline{N}^2 - N_0^2) \times 10^{-4}$ s^{-2} with h_s = 30 m.

that the location of the position of maximum vertical velocity varies between constituents over quite short distances. To quantify this and see how it is affected by the presence of a second sill, vertical velocity power spectra integrated over the whole depth were computed at x = 250 m and 750 m (midway between sills when L = 1.5 km; see Figure 5). Power spectra at x = 250 m (Figure 4a) reveal that at this location, power at the M_8, M_{10}, and M_{12} frequencies is larger than the M_2, M_4, or M_6 frequency. At first sight this appears strange in that one might expect maximum power at the fundamental (M_2) frequency, since this is the forcing frequency, with other harmonics generated from it by flow over the sill when $U_0/(\omega a_s) > 1$ (LK08) and the nonlinear wave-wave interaction. In addition. it has on average the largest u-current amplitude in the region (Figure 3a). However, for the w component of velocity its maximum amplitude occurs at about x = 100 m, with a minimum for M_2 at x = 250 m (Figure 3c), whereas there is a maximum at x = 250 m for M_8, M_{10}, and M_{12} tides (Figure 3c). At x = 750 m, the M_2 component contains more power than the higher harmonics (Figure 4b), due to the different spatial distributions (Figure 3c).

[19] As discussed previously, although the model cannot accurately determine the level of mixing in the sill region, it can show areas of critical Richardson number (taken here as values below 0.25 to be consistent with oceanographic measurements, although all values are given). In these regions there is the potential for enhanced mixing to occur. It is evident from the tidally averaged distribution of Richardson numbers and temperature fields (Figure 5a) that the temperature distribution at about midwater has changed from its initial distribution. This change occurs in the region of critical Richardson number (Figure 5a) and is associated with enhanced mixing at about midwater. In order to quantify how much mixing has occurred over the first seven tidal cycles, the parameter $DN = \overline{N}^2 - N_0^2$ was computed (Figure 5b), with N_0 the initial buoyancy frequency and N^2 its tidally averaged value centered at t = 6.5T. By averaging over a tidal cycle, changes in density due to tidal advection can be removed. As the density field over the whole domain is saved at 10 min intervals, this change in density is computed more accurately than is possible from observations where only a limited number of locations and time values are recorded.

[20] Contours of DN (Figure 5b) clearly show that there has been substantial midwater mixing at about z = −45 m on either side of the sill, as inferred from the change in temperature surfaces shown in Figures 2a, 2b, and 2c. This mixing is largest close to the sill and decreases with distance downstream of it. The vertical location of this mixing corresponds to the region of largest vertical displacement (Figure 3c) and shear (as shown by the vertical phase change (Figure 3b)) of the M_2 internal tide. In addition, it coincides with the region of generation of higher harmonics of the tide (Figure 3a). The short wave nature of these tides and their slow propagation away from their generation region suggests that they may have a significant contribution to the mixing. The effect of this increase in midwater mixing is to reduce the vertical temperature gradient by mixing water into the regions from above and below it, leading to local increases in vertical temperature gradients and an increase in DN as shown in Figure 5b.

3.2. Double-Sill Calculation (Calc 2), U_o = 0.1 m s^{-1}, h_s = 30 m

[21] For the calculation involving two sills separated by L = 1.5 km (Calc 2), a typical sill separation found in the Ringdals Fjord–Idefjord systems [*Johnsson et al.*, 2007], it is evident that at t = 56/8T (Figure 2a) a region of intensified u tidal current at z = −20 m has developed between the two sills. Such a tidal intensification was not found on the right-hand side of the single sill (Calc 1, Figure 2a). In addition, the distribution of the isotherms on the right-hand side of the left sill (namely, the sill located at x = 0 m) has changed from that found in the single-sill problem (Figure 2a). Similarly at t = 58/8T (Figure 2b), although there is an intense jet that leaves the top of the right-hand sill (namely, the sill at x = 1500 m) which is comparable to that found in the single-sill calculation, such a jet does not occur on the right-hand side of the sill at x = 0. In essence, the presence of the second sill inhibits the generation of this

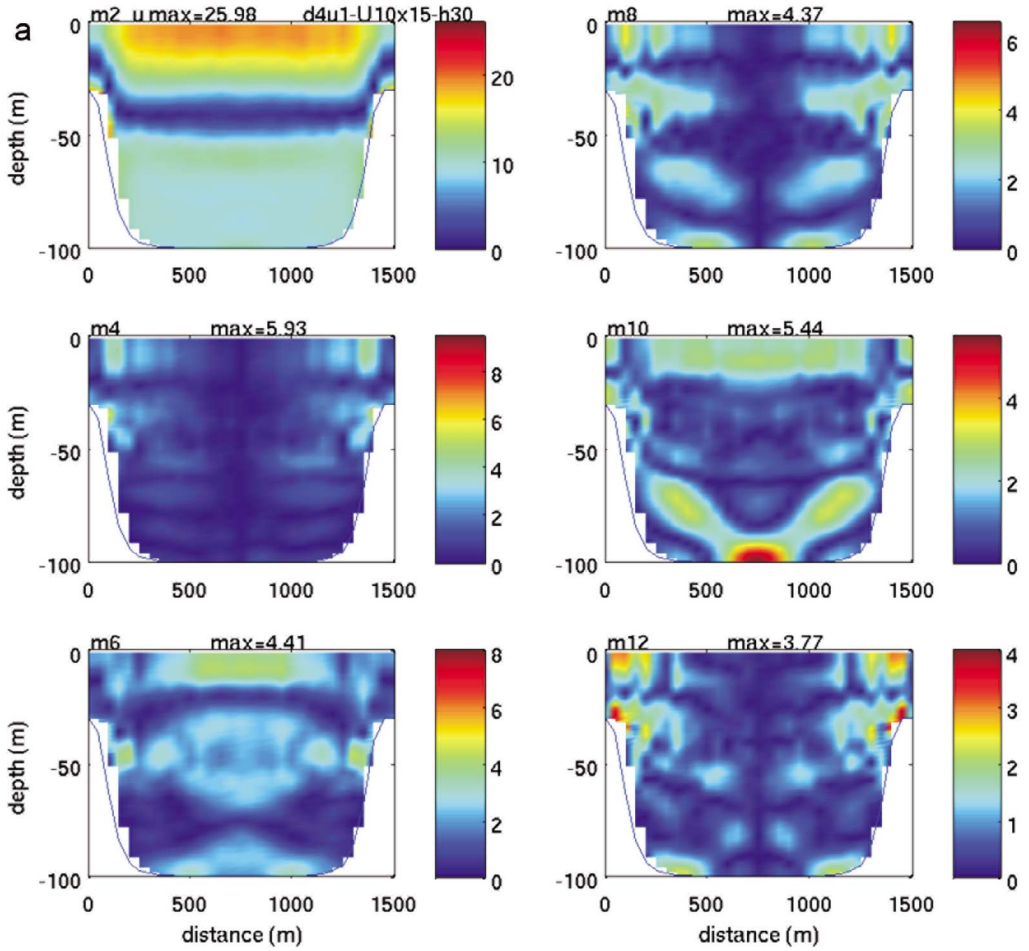

Figure 6. (a) Subdomain of the sill region showing amplitude (cm s^{-1}) of the u component of the baroclinic velocity for the M_2 to M_{12} tidal constituents, for the double sill case with L = 1.5 km and h_s = 30 m. (b) As in Figure 6a but for phase (degrees).

jet. A similar effect occurs half a tidal cycle later (t = 62/8T) (Figure 2c) where a jet occurs on the left-hand side of the sill at x = 0), as in the single-sill case (Figure 2c) although not on the left-hand side of the sill at x = 1500 m. In terms of the "jet-like" response of the sill, this clearly shows that it has been appreciably modified by the presence of the second sill. Since this "jet-like" response is significant in determining mixing in the near-sill region, then this cannot simply be determined by regarding it as the linear sum from each sill; their interaction is very important. Sill interaction in terms of the "wave-like" response is considered later. In terms of the "far-field" propagation of the internal tide (not presented), this is not substantially different from the single-sill calculation, shown in Figure 1a. Consequently, this change in the jet intensity in the intersill region compared to the single-sill calculation clearly shows that there is interaction between the sills.

[22] Contours of Richardson number and DN clearly show (Figures 5a and 5b) that the change in the initial and final density field in the region between the sills in the two sill calculation is different to that found with one sill. In particular, comparison of the Richardson number distributions between the one- and two-sill cases shows that the region of critical Richardson number between the sills has increased in the two-sill calculation. In addition, the midwater separation of the isotherms has increased, as shown in the DN distributions (Figure 5b). Contours of DN (Figure 5b) over the seventh tidal cycle show that there has been a substantial increase in midwater (centered at z = −45 m) mixing between the two sills (Figure 5b), compared to the single-sill case. Not only is the mixing increased but its horizontal spatial distribution between the sills is uniform compared to the single-sill case. However, outside the region between the sills it decays with distance from the sill. This distribution is consistent with the single-sill case. Figures 5a and 5b clearly show that there is significant interaction between the two sills, which influences the current and mixing between the sills, although the "far-field" large-scale internal tide response and even the jet on the outer sides of the sills is not significantly influenced by the presence of one or two sills. The extent to which the mixing between the sills is influenced by the presence of the second sill is examined later in more detail in terms of the sill separation distance.

[23] Since the "outer solution," namely, that beyond the two sills, is not influenced by the presence of the second sill, we will consider here the "inner solution," namely, that between the sill and the spatial distribution of tidal harmonics in the region, namely, the "wave-like" response to the

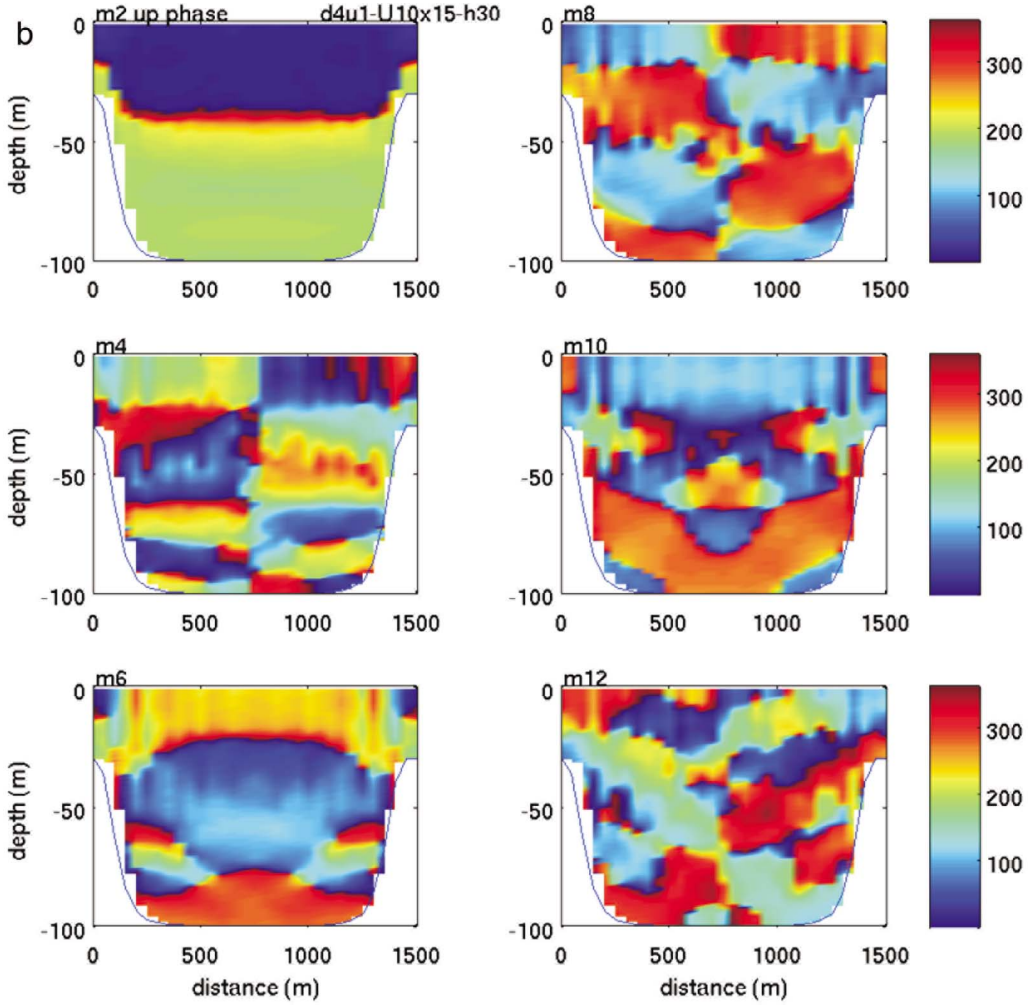

Figure 6. (continued)

presence of the second sill. Unlike in the single-sill calculation where the u current amplitude at the M_2 frequency in the surface layer was a maximum close to the sill at x = 0 (Figure 3a), in the two-sill case the maximum is between the sills, although still at the sea surface (Figure 6a). As previously (Figure 3a), there is a midwater region where the M_2 internal tide is near zero (although this has been displaced slightly upward in the vertical; compare Figures 3a and 6a). Below this the u current amplitude is of the order of 10 cm s^{-1}, reducing as the near-bed region is approached (Figure 6a). This suggests a vertical structure composed of both first and second internal modes. However, a 180° phase change in the vertical was found for the M_2 tide (Figure 6b), suggesting that the first mode dominated. For the higher harmonics of the tide, there are significant phase changes in the vertical (Figure 6b), showing the presence of higher vertical modes.

[24] The M_2, M_6, and M_{10} harmonics exhibited a maximum u current amplitude at x = 750 m, midway between the two sills, although the vertical position of this changes from surface (M_2 and M_6) to bed (M_{10}). In the case of the other harmonics, namely, M_4, M_8, and M_{12}, they are zero along the centerline. This suggests constructive and destructive interference of the internal waves that propagate from each sill, in a similar manner to internal seiche motion in a lake [*Hall and Davies*, 2005]. A set of standing internal waves is generated, with the first horizontal mode (the internal M_2 tide) having a maximum at the midpoint between the sills. The second mode (M_4 tide) has a minimum at x = 750 m, between the two maxima that appear close to the sill top. Higher modes with alternate maxima (M_6, M_{10}, etc.) and minima (M_8, M_{12}, etc.) at x = 750 m and an increasing number of maxima and minima in the horizontal are evident (Figure 6a). Associated with these horizontal modes are vertical modes of increasing vertical structure (Figure 6a). In summary, in the case of the higher harmonics of the M_2 tide, they show appreciable horizontal and vertical variability reflecting their shorter wavelength and generation of higher vertical modes. In essence, propagating internal waves from each sill combine to form a standing internal wave.

[25] Associated with the standing wave, there is a nodal point in w at the center of the basin region between the sills where u is a maximum for the frequency M_{2n}, with n odd. This is evident in the power spectra of w at the center of the region (Figure 4d) where there is no peak at the M_2, M_6, M_{10}, etc., frequency. This is appreciably different to that

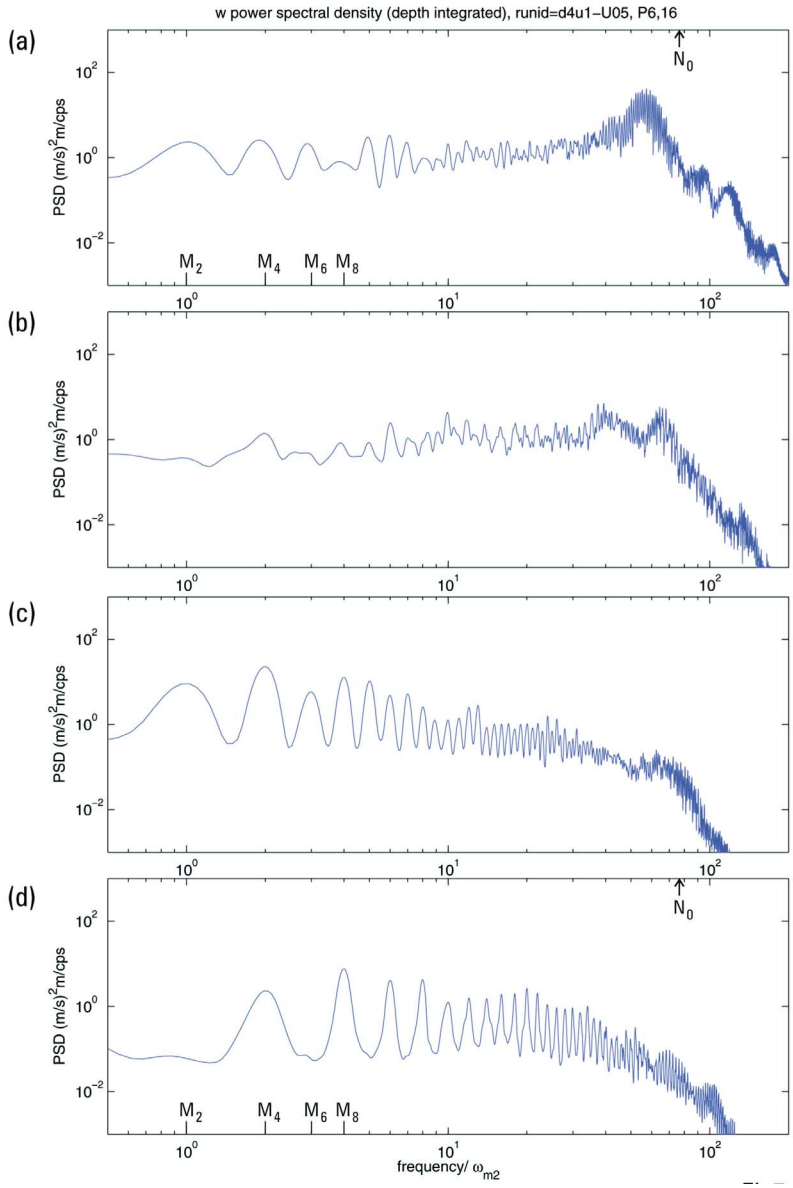

Figure 7. Power spectra of the vertical velocity, integrated through depth, normalized with respect to the M_2 tide at (a) x = 250 m and (b) x = 750 m for the double sill case (L = 1.5 km), computed with h_s = 15 m and U_0 = 0.05 m s^{-1}, and (c) x = 250 m and (d) x = 750 m, computed with h_s = 60 m and U_0 = 0.1 ms^{-1}. Note that horizontal axis shows frequency relative to the M_2 tidal frequency (ω_{M2}), i.e., f/ω_{M2}; hence 10° indicates the M_2 frequency. Also marked is initial buoyancy frequency N_0.

found previously (Figure 4b) where there was energy at all higher harmonics of M_2.

[26] As in the single-sill case, power spectra show a dropoff in energy at higher frequencies than those associated with the internal tide. For spectra close to the sill, i.e., x = 250 (Figure 4c), there is an increase at the lee wave period (with frequency of order 70 times M_2 tidal and close to the initial buoyancy frequency N_0, as marked in Figure 4). In addition, there is less energy in the overall internal wave spectrum for the two sill than the one-sill problem. This will be considered later in terms of a comparison of energy flux calculations for the one- and two-sill cases.

[27] The change in nature of the internal tide between the sills from a progressive to standing wave, due to wave reflection from each sill, suggests a possible mechanism for the enhanced mixing found between sills [*Johnsson et al.*, 2007]. Associated with internal wave reflection, as occurs here to form a standing wave, *Eriksen* [1985] showed there is a significant increase in vertical shear and associated mixing. In the present case, short wave higher harmonics of the internal tide are generated and "captured" between the sills. Consequently, internal wave energy cannot propagate away from the intersill region, giving rise to a region of reduced Richardson number (Figure 5b). The region where the Richardson number falls below its critical value and hence there is enhanced mixing (quantified by the DN distribution) is increased compared to the single-sill case (see Figures 5a and 5b). Hence the generation of short waves that

are "captured" between the sills as a standing wave explains the enhanced mixing found in such regions [Johnsson *et al.*, 2007]. In section 5 the effect of intersill separation distance L upon the magnitude of short waves and hence the level of mixing is considered in terms of resonance.

3.3. Effect of Sill Height and Tidal Velocity

[28] Here the effect of sill depth (h_s) and tidal velocity (U_0) is very briefly considered. More detailed studies of the response of a single sill [e.g., *Baines*, 1995; XD06; XD07; LK08] have shown that since these affect the Froude number, they also influence the internal tide and mixing at a single sill. By briefly examining the two-sill response to the range of parameters that usually occurs in two sill situations, the generality of the previous results can be considered.

3.3.1. Double-Sill Calculation (Reduced Sill Depth) (Calc 3), $U_o = 0.1$ m s^{-1}, $h_s = 15$ m

[29] For a single sill the effect of reducing h_s to 15 m, while maintaining $U_o = 0.1$ m s^{-1}, is to appreciably increase the across sill Froude number $F_s = U_s/Nh_s$, giving rise to a larger hydraulic transition, and appreciable overturning and mixing in the upper part of the water column.

[30] In the double-sill case the hydraulic transition that occurred in the single-sill case is not present. This suggests that interaction increases as F_r increases, leading as before to more mixing in the two-sill case than in the one-sill case.

3.3.2. Double-Sill Calculation (Calc 4) (Reduced Forcing), $U_o = 0.05$ m s^{-1}, $h_s = 15$ m

[31] To examine a reduction in Froude number and U/h, while still maintaining a shallow sill depth, the tidal forcing was reduced to $U_o = 0.05$ m s^{-1} with a substantial decrease in lee waves (see LK0; K10) and mixing. However, as in earlier calculations the presence of the second sill leads to a standing wave internal tide and an associated change in mixing, which modifies the distribution of internal tidal beams and hence the internal tide.

[32] In the case of the sill depth $h_s = 15$ m, power spectra (Figure 7a and 7b) show appreciably less power in the lower-frequency tidal harmonic range of the spectrum, with a peak at the lee wave frequency. This is consistent with DX06, who found that for a steep sill (the case considered here) as h_s decreased, leading to an increased across sill velocity U_s and hence U_s/N, the energy in the lee wave band increased compared to that in the internal wave band and mixing was enhanced. This increase in lee wave energy in the sill region (DX06) with U_s/N is consistent with the oceanic solutions of LK08 and K10. As in the other calculations there are only peaks at the M_{n2}, for n even, at x = 750 m. In essence, as sill height is increased, reducing sill depth h_s, more of the barotropic tidal energy is converted into lee wave energy than internal tide energy.

3.3.3. Double-Sill Calculation (Calc 5) (Increased Sill Depth), $U_o = 0.1$ m s^{-1}, $h_s = 60$ m

[33] The effect of an increased sill depth, $h_s = 60$ m while maintaining $U_o = 0.1$ m s^{-1} is to slightly reduce the maximum across sill velocity and hence the parameter U_s/N. This leads to a decrease in lee wave activity and mixing on the lee side of the sill (not shown), compared to previously (Figures 5a and 5b).

[34] Contours of the amplitude of the u component of the M_2 internal tide (not presented) show that unlike in previous two-sill calculations (Calcs 2, 3, 4) it is a maximum at depth, just above the seabed, compared with the surface maximum shown previously (see Figure 6). This suggests that the M_2 internal tidal energy propagates downward. However, in the sill area and near the surface there are regions of increased amplitude associated with upward propagating internal tidal energy. At the M_4 frequency there are local sea surface maxima slightly offset from the top of each sill. Associated with these maxima are others at identical horizontal positions but farther down in the water column, suggesting that high vertical modes are present at these positions.

[35] As for $h_s = 30$ m, power spectra of the vertical velocity at x = 250 m and 750 m showed the presence of energy at all tidal harmonics at x = 250 m (Figure 7c) and only at M_{n2} (for n even) at x = 750 m (Figure 7d). The decrease in U_s and F_s, diminished lee wave generation as shown by the reduction in the energy peak at about 70 ω_{m2} (compare Figures 4c and 7c). This also gave rise to a reduction in vertical mixing. As previously, there was still appreciable interaction between the two sills.

4. Influence of Sill Separation (L) Upon the Internal Tide and Energy Flux

4.1. Influence of Sill Separation Upon Internal Waves

[36] In section 3 the separation between the sills was fixed at L = 1.5 km, and the influence of h_s, U_s/N and F_r was examined. Here the influence of sill separation L, is examined for the case in which $h_s = 30$ m with $U_o = 0.1$ ms^{-1}, and with L taking values of 2.5 km, 5.0 km, and 10.0 km. As before, the domain between x = 0 and 2000 m is considered in detail.

[37] As previously, when L = 1.5 km (Calc 2) the effect of the second sill at L = 2.5 km (Calc 6) is to modify the lee wave response on the right-hand side of the sill at x = 0 compared with the single-sill calculation (e.g., see solutions at t = 56/8T, Figure 8a (L = 2.5 km) and Figure 2a). This clearly shows that there is interaction between the sills even when L = 2.5 km that influences not only the internal tide response but also the lee wave intensity. In addition, the strong jet that leaves the sill top at t = 58/8T in the single-sill case (Figure 2b) is no longer present. At other times the solution (not presented) is comparable to that computed with L = 1.5 km, although the midwater mixing is reduced.

[38] As the sill separation is increased to L = 5.0 km (Calc 7), the solution at t = 56/8T in the region of the sill at x = 0 shows (Figure 8b) a similar vertical displacement of the isopycnals and currents associated with the lee waves to those found in the single-sill case (Figure 2a). In addition at t = 58/8T (not presented) a weak jet is evident that separates from the top of the sill. In terms of the "outer region" distribution of the M_2 internal tide (not presented), this is not significantly influenced by the sill separation distance L.

[39] When the sill separation is increased to L = 10 km, it is evident from Figures 8c and 2a that although the lee wave distribution adjacent to the sill is comparable to the single-sill case (Figure 2a), the near-surface tidal current away from the sill is appreciably increased. A significant enhancement in surface current compared to the single-sill calculation is evident at t = 58/8 T with a marked reduction in the intensity of the jet leaving the top of the sill (not presented). The reason for these changes in the tidal

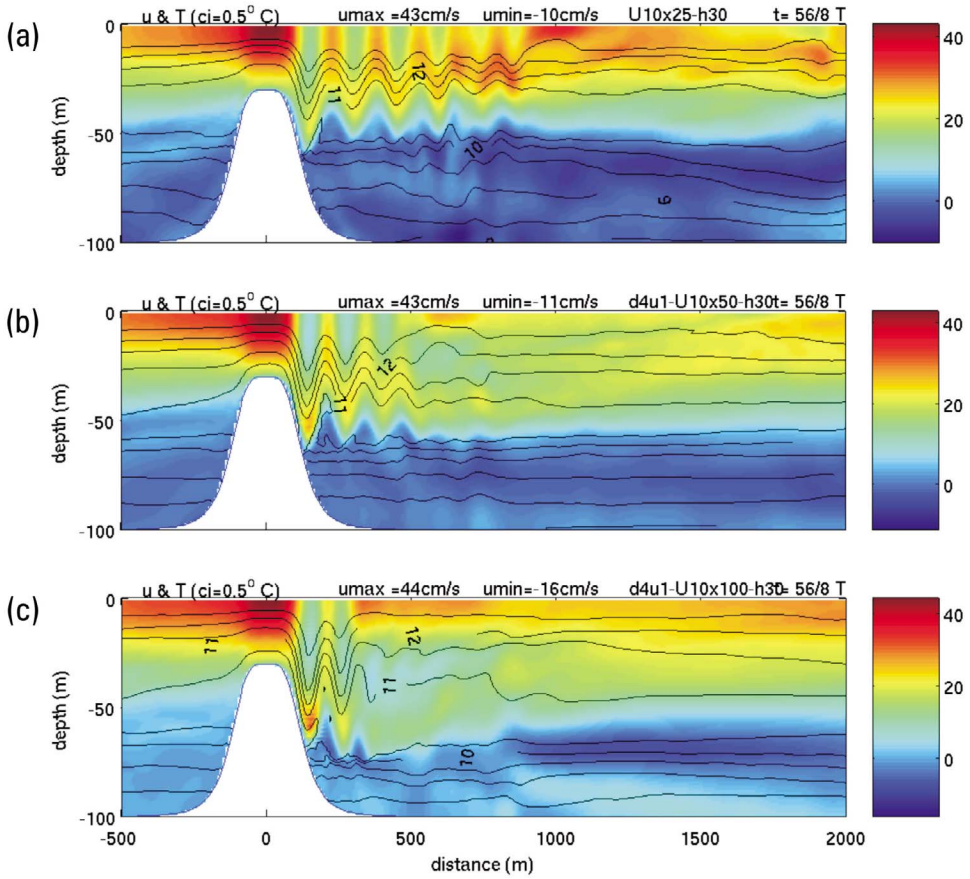

Figure 8. Subdomain of the region close to the sill at x = 0, with h_s = 30 m, showing velocity u (cm s^{-1}) and temperature field (°C, c.i. = 0.5°) for the double sill case at t = 56/8T, for (a) L = 2.5 km, (b) L = 5.0 km, and (c) L = 10.0 km.

distribution at the sill can be appreciated from the "far-field" "snapshot" picture of the tide (Figure 1b). Calculations showed that an increase in L from 1.5 km to 5 km only has a small effect upon the "far field" tidal distribution. However, when L is increased from 5 km to 10 km this "far-field" distribution changes with an associated increase in the intensity of the internal tide between the two sills (see Figure 1b). This implies that when the sill separation L is small (of order less than 5 km) compared to the horizontal wavelengths of the internal tide (of order 25 km), then the influence of the two sills upon the "far-field" tidal distribution is small. However, when L = 10 km, the internal

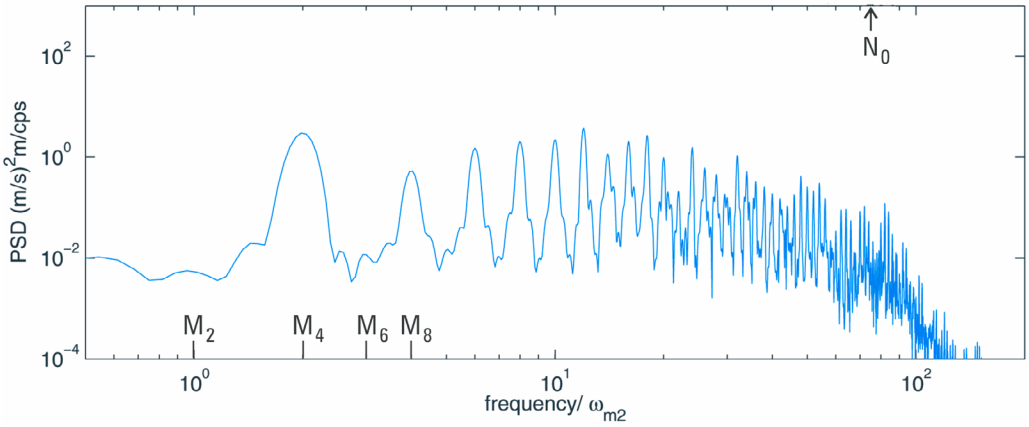

Figure 9. Power spectra of the vertical velocity integrated through depth, normalized with respect to the M_2 tide at x = 750 m in the double-sill case with L = 5.0 km and h_s = 30 m.

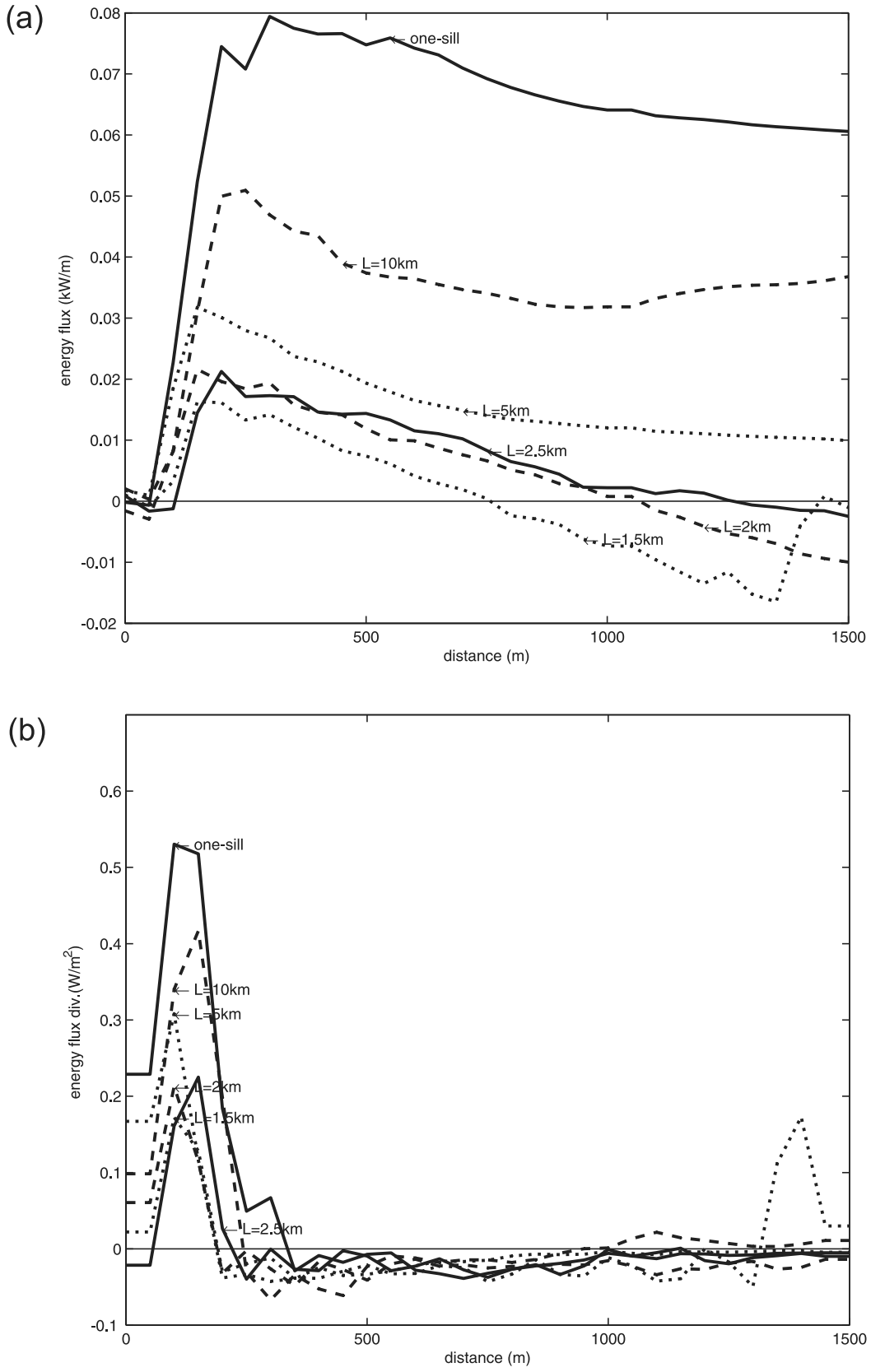

Figure 10. (a) Tidally averaged energy flux (kW/m) in the two sill case for L = 1.5 km (dotted line), L = 2 km (dashed line), L = 2.5 km (solid line), L = 5 km (dotted line), L = 10 km (dashed line) and also the single sill case (solid line), computed with h_s = 30 m, and (b) as Figure 10a but for energy flux divergence.

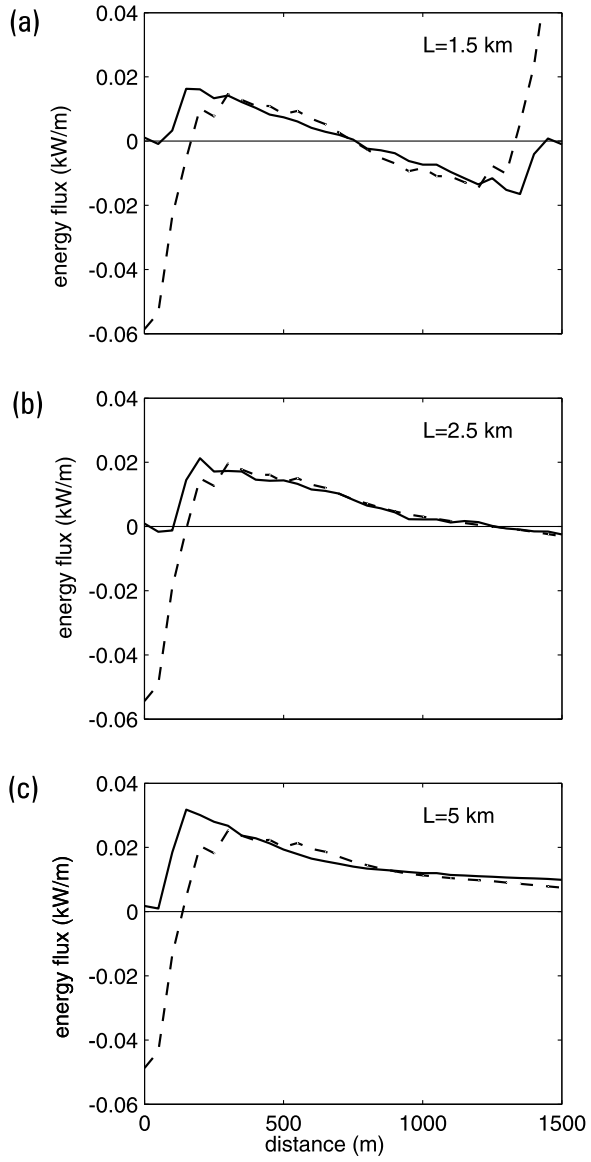

Figure 11. Tidally averaged energy flux in the two sill case (solid line) and that determined by linearly superimposing the single-sill energy flux (dashed line) for (a) L = 1.5 km, (b) L = 2.5 km, and (c) L = 5 km.

tide is influenced by the two sills and both the "inner" and "outer" tidal solutions are modified.

[40] As in the previous calculation with L = 1.5, for the L values considered here, the power spectrum in the center of the "inner region" shows that a standing wave is present with appreciable energy only in the M_{n2} (for n even) harmonics (Figure 9). However, the energy distribution between the various harmonics does vary depending upon intersill separation distance L (compare Figures 4d and 9). This suggests that depending upon the value of L, the magnitude of a particular constituent may increase or decrease due to resonance. This is considered later in the paper.

4.2. Influence of Sill Separation Upon Energy Flux

[41] To quantify the extent to which the sill separation distance L influences the interaction between the sills, vertically integrated values of the energy flux (Figure 10a) and its divergence (Figure 10b) were derived by time averaging over tidal cycles seven and eight. Owing to dissipation between the sills, which is shown by *Johnsson et al.* [2007] to be significant, then in the limit as L increases, interaction between the sills will be reduced, and the energy flux from each sill will approach that of an isolated sill. Calculations were performed for a single sill and double sill for L = 1.5, 2, 2.5, 5, and 10 km. In these calculations the sill depth h_s = 30 m. Since the internal wave energy flux is directed away from the sill, then in the two-sill case the energy flux is antisymmetric with respect to the center point between the sills, namely, x = 750 m for L = 1.5 km (Figure 10a), with the energy flux divergence symmetric about this point, and having a maximum close to each of the sills. These distributions were also found as L was increased, but since only the 1500 m region on the right of the first sill (i.e., that at x = 0) is given in Figures 10a and 10b, it is not evident. However, Figures 10a and 10b clearly show that as L is increased the magnitude of the energy flux and its divergence increase, approaching the single-sill value, as to be expected in the limit that L goes to infinity.

[42] If there was no interaction between the sills, then the energy flux in the region between them could be obtained by a simple linear combination of that due to each sill, taking account of the direction of the flux. Considering initially the case of L = 1.5 km (Figure 11a) in the region away from each sill, this linear approximation is in good agreement with that found in the two sill calculation and shows a linear decay with distance from each sill. However, in the near-sill region where nonlinear effects are important and there is a significant conversion of energy into the internal tide, this linear superposition is invalid. Obviously, as L increases the linear superposition becomes more valid, as shown by the decrease in the energy flux error (difference between the true solution and linear combination) at x = 0 as L increases from 1.5 km to 5 km (Figures 11a, 11b, and 11c). This suggests that in terms of energy conversion from the baroclinic tide to mixing in the near-sill region, it is important to account for how it is affected by the presence of the second sill and not to linearly combine each separate sill solution.

4.3. Influence of Sill Separation Upon Mixing

[43] Although the calculation of how the energy flux varies with separation L reveals the degree of nonlinear interaction, in the work of *Johnsson et al.* [2007] the emphasis was placed on mixing in the midwater region. To examine how this changes as L varies, it is valuable

Table 2. Values of DNA for a Single-Sill Case and Two Sills Separated by a Distance L Forced With the M_{10} Tide[a]

L, km	DNA, s^{-2}
Single	0.3579
10	0.3677
5	0.3679
2.5	0.5387
2.0	0.5580
1.5	0.5988

[a]DNA is the mean area integral of DN where $\overline{N}^2 - N_0^2$ with N_0 the initial buoyancy frequency and N its tidally averaged value (see equation (2)).

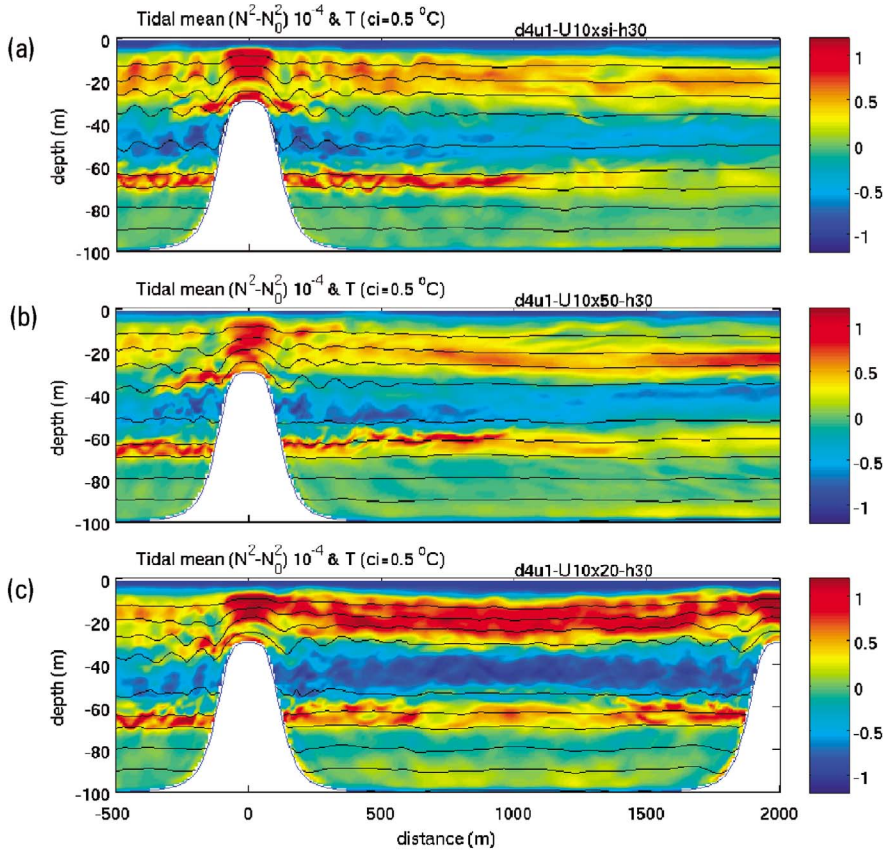

Figure 12. Tidal mean $DN = (\overline{N}^2 - N_0^2) \times 10^{-4}$ s^{-2} and temperature contours (°C) for (a) a single sill, (b) two sills with L = 5 km, and (c) L = 2 km, computed with M10 tidal forcing.

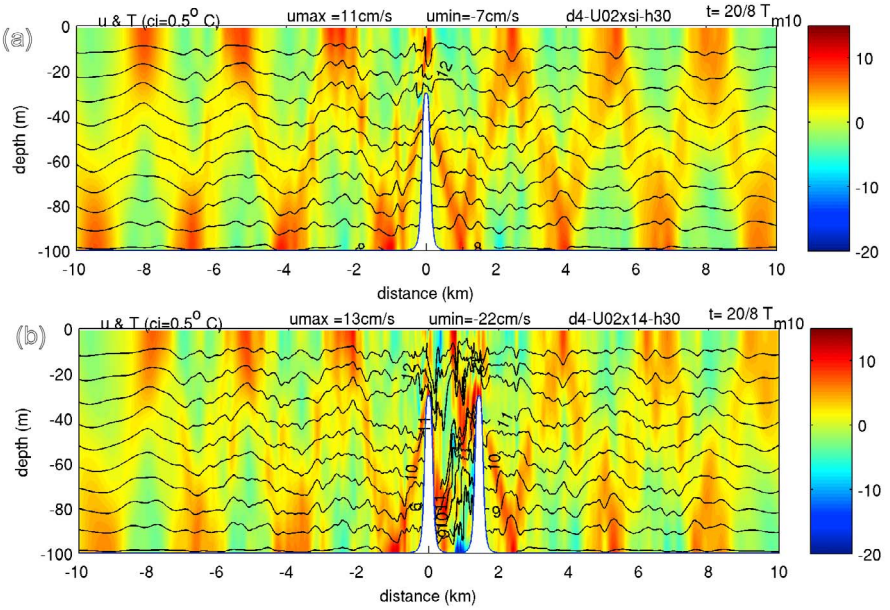

Figure 13. (a) Subdomain of the sill region, i.e., x = −10 km to 10 km showing a single sill at x = 0, temperature field (°C, c.i. = 0.5°C), and the u velocity (cm s^{-1}) after 20 M_{10} tidal cycles, induced by a barotropic M_{10} tidal forcing U_0 = 0.02 ms^{-1} and (b) two sills with L = 1.44 km.

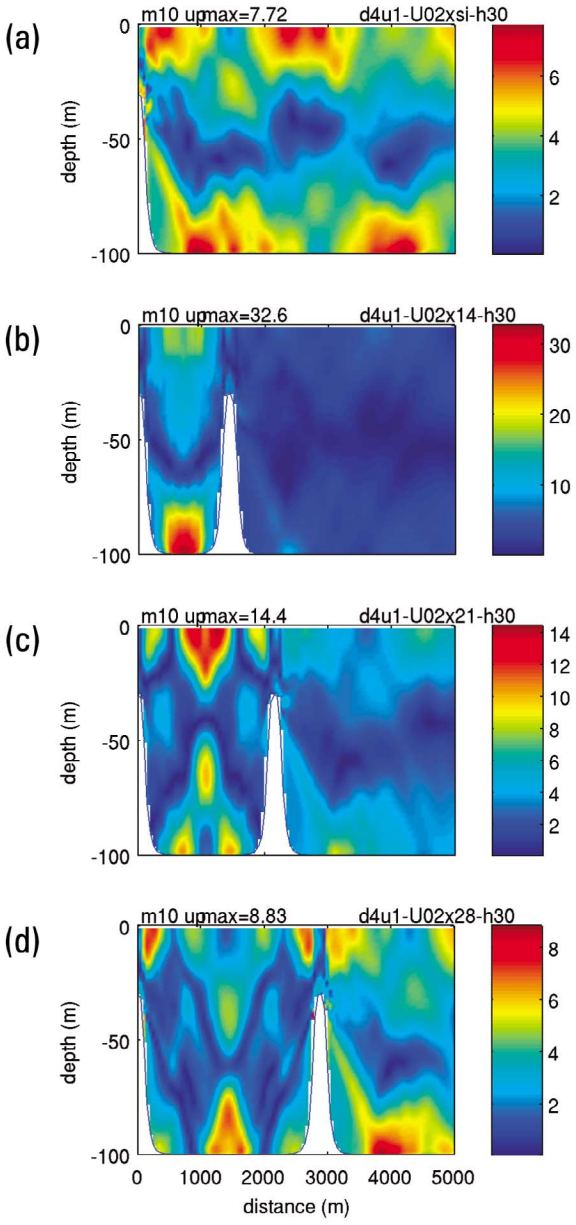

Figure 14. Subdomain of the sill region, showing amplitude of the M_{10} harmonic for (a) a single sill, and two sills separated by (b) L = 1.44 km, R = 0.5, (c) L = 2.16 km, R = 0.75, (d) L = 2.88 km, R = 1.0, where R = L/λ_h, with λ_h the horizontal wavelength of the M_{10} harmonic.

to consider changes in the mean area integral of DN (DNA) over this midwater region, i.e., from Z = −55 to −30 m (Δz) and the area adjacent to the sill, i.e., from x = 0 to 750 m (Δx), and thus

$$DNA = \frac{1}{\Delta x \Delta z} \int_0^{750} \int_{-55}^{-30} DN dx dz. \quad (2)$$

[44] Consequently, DNA is a measure of the midwater mixing in the sill region as the intersill separation L changes. Values of DNA (Table 2) show that mixing changes very little from the single-sill case when L = 10 km or 5 km. However, when L is reduced to 2.5 km or less, there is an appreciable increase in mixing. These changes are clearly evident from the DN distributions and temperature contours shown in Figures 12a, 12b, and 12c. From a comparison of DN distributions between x = 0 and 750 m in Figures 12a (single sill) and Figure 12b (sill at 5 km), it is evident that there are no substantial differences, although the effect of the second sill is seen in the region from x = 1500 to 2000 m. However, when L is reduced to 2000 m (Figure 12c), there is enhanced mixing in the region of the first sill due to its presence. In essence, the mixing at the first sill is increased nearly twofold due to the presence of the second sill. This clearly shows that for values of L of order 5 km or above, total mixing can be computed as the linear sum of that due to each sill as in the work of *Johnsson et al.* [2007]. However, below this value this is not possible due to interaction.

5. Resonant Effects

[45] As discussed previously, for a first mode baroclinic tide at the M_2 period the horizontal wavelength for the parameters used here is of the order of 27 km. Consequently, for the typical sill separations considered here, i.e., up to 10 km, the M_2 wavelength far exceeds the intersill distance. However, for higher harmonics of the tide, the horizontal wavelength of the first mode is 4.94 km (M_6), 3.64 (M_8), and 2.88 km (M_{10}) and hence shorter than the intersill separation. Since it is the shorter-wavelength waves which are most prone to breaking and hence contribute most to the mixing, then it is instructive to examine the extent to which these are amplified by trapping between the sills. As shown earlier, the power spectra (Figures 4d and 9) show that the amplitude of the various harmonics changes as L is varied. This suggests a resonant type amplification when the intersill separation is varied as a factor of the first mode horizontal wavelength. This is illustrated here for the M_{10} component of the tide, although the other harmonics exhibit comparable effects. It is evident from Figure 6, in particular, the phase distribution in the vertical, that when M_{10} is generated from the M_2 tide that besides the first mode, higher vertical modes are produced with associated shorter wavelengths. In addition, as shown previously, there is extensive mixing in the problem and this will change the internal wavelength and lead to a broadening of any resonance frequency and the raypaths of internal tide propagation. This in turn will reduce internal tide focusing and the concentration of energy on wave attractors [*Maas and Lam*, 1995]. In order to minimize these effects and clearly illustrate how variations in intersill separation can enhance internal wave energy, it is necessary ideally to generate just a first mode baroclinic internal tide in the absence of other harmonics and modes. To this end, the model domain, stratification, and water depth were as previously but the body force was applied at the M_{10} rather than the M_2 frequency. In addition, its amplitude U_0 was reduced to 0.02 ms^{-1} in order to minimize nonlinear effects, and hence the generation of short internal waves, with associated nonlinear effects and mixing.

[46] A snapshot of the current field and temperature distribution after 20 M_{10} tidal cycles for a single sill

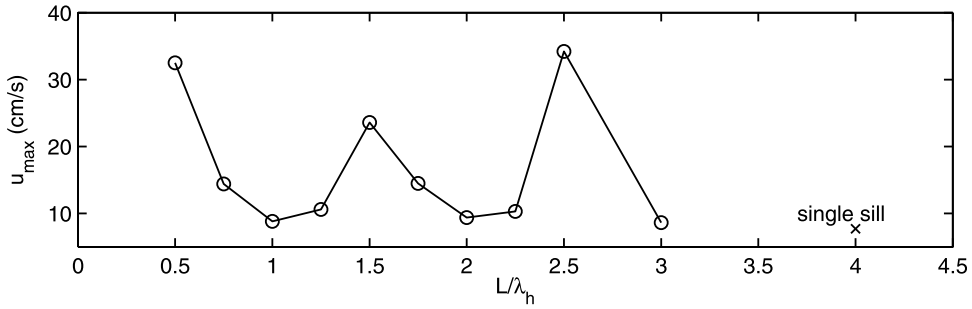

Figure 15. Maximum M_{10} U current amplitude (U_{max}) (cm s^{-1}) for various values of $R = L/\lambda_h$, with λ_h the horizontal wavelength of the M_{10} harmonic.

(Figure 13a) shows that this approach has been fairly successful, in that tidal beams corresponding to a first mode baroclinic internal tide of wavelength 2.88 km are generated on either side of the sill. However, isotherms close to the sill show the presence of short waves, and the broadening of the tidal beams suggests that mixing and damping have occurred as the internal tide propagates away from the generation region. A harmonic analysis of the u current in the near-sill region (Figure 14a, phase not shown) shows the presence of a first mode wave, having a wavelength of order 3 km.

[47] In a subsequent calculation a second sill was placed at L = 1.44 km (i.e., half the M_{10} wavelength). From the snapshot (Figure 13b) it is evident that this increases the magnitude of the near-bottom current in the intersill region. In addition, there is more short wave generation and mixing giving rise to broader tidal beams (Figure 13b). This suggests that there may be more focusing of the internal tidal wave in the intersill region, giving rise to stronger currents. The intensification of the current in the near-bed region was confirmed by the harmonic analysis (Figure 14b). This shows a significantly stronger current amplitude than found in the single-sill case, namely, 32.6 cm s^{-1} compared to 7.7 cm s^{-1}, confirming that at these distances short internal wave energy is trapped between the sills and there is significant interaction between these short-wavelength waves.

[48] To examine to what extent the ratio $R = L/\lambda_h$, with λ_h the horizontal wavelength of the M_{10} constituent influences the magnitude of current amplitude, and hence when focusing may occur leading to a peak in current magnitude, calculations were performed with a range of R values. For each R value the maximum u current amplitude (U_{max}) was determined in the intersill region, and this was plotted against R (Figure 15). It is evident from Figures 14b–14d that the position of this value varied depending upon R. From Figure 15 it is apparent that a maximum value of U_{max} occurs when R = 0.5. In this case the two sills are close, there is little energy loss by damping, and the tidal beams appear more focused and constructively interfere with each other to give a single maxima in the near-bed region between the sills (Figure 14b). At R = 0.75 a more complex distribution occurs (Figure 14c) with the maximum in the surface layer and some evidence of higher vertical modes. The distribution at R = 1.0 (Figure 14d) is comparable to that found at R = 0.5 (Figure 14b) although with a significantly reduced amplitude. It is apparent from Figure 15 that the next maximum amplitude occurs at R = 1.5. This is associated with the presence of higher horizontal and vertical modes (not shown).

[49] Further increases in L show (Figure 15) that U_{max} is a maximum for R = 0.5, 1.5, and 2.5, suggesting that resonance is occurring as the internal tides generated at each sill constructively interfere with each other and there appears to be some wave focusing. The damping of internal wave energy due to viscous and diffuse effects, and the fact that mixing is occurring in the intersill region means that the tidal energy beams are not as highly focused as in the analytical work of *Nycander* [2005, 2006] and *Balmforth and Peacock* [2009]. Consequently, the focusing of beams along attractors is much more diffuse than in the work of *Maas and Lam* [1995] and *Drijfhout and Maas* [2007]. However, Figure 15 shows that for integer R values the U_{max} is a minimum while at in-between values it is a maximum. The extent to which focusing of internal tide energy along attractors leads to enhancement of internal tide energy at certain intersill separations L is difficult to clearly establish, although there are clear peaks and troughs in the U amplitude as L changes. In addition, the focusing of internal tides means that the tidal beams in these regions will constructively interfere with each other, leading to U_{max} values that are never less than those found in the single-sill case. This appears to occur here where U_{max} in Figure 15 never falls below the single sill value.

6. Summary and Conclusions

[50] Calculations have been performed using idealized topography and sills in a loch/fjord region to determine the influence of sill depth h_s, tidal current U_0, and sill separation L upon tidally forced internal wave generation in the region. In all cases the water depth h and initial buoyancy frequency N were fixed, although h_s and tidal forcing varied. Initial calculations using a single sill showed that for small values of h_s, of order 15 m, strong lee waves, a tidal jet, and significant mixing occurred on the lee side of a sill. As sill depth was increased, the lee wave signal and internal mixing was reduced, although a significant internal tide at the M_2 frequency was still produced, and gave rise to an appreciable energy flux away from the sill. In addition to the fundamental (M_2 component) tide, higher harmonics with

a shorter horizontal and vertical wavelength were generated. Their intensity and spatial distribution were examined using power spectra of the vertical velocity.

[51] The introduction of a second sill gave rise to standing internal tidal waves in the region between the two sills. Calculations showed that the spatial distribution of the u current magnitude and phase associated with this wave varied from one harmonic to another. In the case of the fundamental (M_2 frequency) and high harmonics (M_{2n} for n odd) the u baroclinic current had a maximum amplitude midway between the sills, with an associated nodal point in the vertical velocity, typical of standing internal waves. The vertical variation of the M_2 tide was characterized by a first mode baroclinic wave, although higher harmonics exhibited higher modes in the vertical. For higher harmonics, namely, M_{2n} (n even), the baroclinic u current amplitude was zero at the midpoint, with the vertical velocity nonzero. Again these harmonics showed significant horizontal and vertical variability in their amplitude, revealing the presence of high vertical modes.

[52] The spatial distribution of baroclinic u current maxima was influenced by sill height h_s and separation L. In addition to producing a standing internal wave between the two sills, the presence of a second sill gave rise to an enhancement in the region where the Richardson number was critical, resulting in an increase in vertical mixing between the sills. This arose because internal tide energy was trapped between the sills. In addition, with the reflection of the internal tide from each sill, there was an increase in shear and mixing. Also, there was a nonlinear cascade of energy to higher frequencies with a resulting increase in mixing. This goes some way to explaining the enhanced vertical mixing observed in fjords in the region between closely spaced sills [*Johnsson et al.*, 2007].

[53] Calculations of energy flux and its divergence showed that in the single-sill case internal waves were generated near the sill top, with a near-constant energy flux away from this region. This was reflected in the rapid increase in energy flux divergence at the top of the sill slope, in the generation region and its near-zero value away from the sill. The magnitude of the energy flux and its maximum divergence decreased as sill depth increased. In the two-sill case, the magnitude of the energy flux and its divergence for all values of h_s was reduced compared to the single-sill case. This arose because of the change in the baroclinic internal wave from progressive to standing. However, as the sill separation distance L increased, then the energy flux and its divergence approached that found in the single-sill case, as would be expected in the limit as L tended to infinity. Comparing the intersill energy flux derived by linearly combining that from two separate sills with that computed from the two-sill problem showed that there was significant interaction in the region of the sills, although this reduced as sill separation increased. Similarly, the mixing and dissipation in the intersill region showed appreciable nonlinear interaction, although this reduced as intersill distance increased.

[54] In essence, the calculations presented here show that for two closely spaced sills the generation of a standing internal tide and its higher harmonics gives rise to increased mixing between the sills as found in observations. As sill separation approaches the wavelength of the internal tide, this effect decreases. In a final section the influence of intersill separation upon the intensity of the internal tide in the intersill region was briefly examined. For the sill separations considered here, these were much shorter than the wavelength of the M_2 baroclinic tide, although larger than some of its higher harmonics, with the M_{10} constituent showing some local intensification. For this reason, and in view of the fact that the short waves contribute most to mixing, the influence of intersill separation upon the amplitude of the M_{10} tidal current was examined in detail to determine how it was modified from a progressive to standing wave by the presence of a second sill and intensified by focusing.

[55] In deep-ocean situations, tidal beams are very narrow and well defined. Under these conditions the energy in the beam can be focused along attractors giving rise to locations of increased internal tidal energy. This suggests that for narrow beams as the topographic separation varies as in a double-ridge case [*Chao et al.*, 2007], then for a given tidal forcing frequency, sill profile, and stratification, the internal tide amplitude will increase and a sharp peak resonance will occur. In the present case the beams are too diffuse and a more broadband type resonance occurs. This has been illustrated here for the M_{10} constituent and a given stratification and water depth. In order to understand the process in more detail. a comprehensive set of calculations is required, which is beyond the scope of this paper.

[56] **Acknowledgments.** The authors are indebted to R. A. Smith for help in preparing diagrams and to L. Parry and E. Ashton for typing the paper. Valuable comments by two anonymous referees are very much appreciated and enhanced the scope of the paper.

References

Allen, G. L., and J. H. Simpson (1998), Reflection of the internal tide in Upper Loch Linnhe, a Scottish Fjord, *Estuarine Coastal Shelf Sci.*, *46*, 683–701, doi:10.1006/ecss.1997.0308.

Baines, P. G. (1995), *Topographic Effects in Stratified Flows*, Cambridge Univ. Press, New York.

Balmforth, N. J., and T. Peacock (2009), Tidal conversion by supercritical topography, *J. Phys. Oceanogr.*, *39*, 1965–1974, doi:10.1175/2009JPO4057.1.

Berntsen, J., and G. K. Furnes (2005), Internal pressure errors in sigma-coordinate ocean models: Sensitivity of the growth of the flow to the time stepping method and possible non-hydrostatic effects, *Cont. Shelf Res.*, *25*, 829–848, doi:10.1016/j.csr.2004.09.025.

Berntsen, J., J. Xing, and G. Alendal (2006), Assessment of non-hydrostatic ocean models using laboratory scale problems, *Cont. Shelf Res.*, *26*, 1433–1447, doi:10.1016/j.csr.2006.02.014.

Berntsen, J., J. Xing, and A. M. Davies (2008), Numerical studies of internal waves at a sill: Sensitivity to horizontal grid size and subgrid scale closure, *Cont. Shelf Res.*, *28*, 1376–1393, doi:10.1016/j.csr.2008.03.029.

Burchard, H., and H. Rennau (2008), Comparative quantification of physical and numerically induced mixing in ocean models, *Ocean Modell.*, *20*, 293–311, doi:10.1016/j.ocemod.2007.10.003.

Carter, G. S., et al. (2008), Energetics of M_2 barotropic-to-baroclinic tidal conversion at the Hawaiian Islands, *J. Phys. Oceanogr.*, *38*, 2205–2223, doi:10.1175/2008JPO3860.1.

Chao, S.-Y., D. S. Ko, R.-C. Lien, and P. T. Shaw (2007), Assessing the west ridge of Luzon Strait as an internal wave radiator, *J. Oceanogr.*, *63*, 897–911, doi:10.1007/s10872-007-0076-8.

Cummins, P. F., and L.-Y. Oey (1997), Simulation of barotropic and baroclinic tides off northern British Columbia, *J. Phys. Oceanogr.*, *27*, 762–781, doi:10.1175/1520-0485(1997)027<0762:SOBABT>2.0.CO;2.

Davies, A. M., J. Xing, and J. Berntsen (2009) Non-hydrostatic and non-linear contributions to the internal wave energy flux in sill regions, 59(6), 881–897, doi:10.1007/s10236-009-0217-2.

Drijfhout, S., and L. R. M. Maas (2007), Impact of channel geometry and rotation on the trapping of internal tides, *J. Phys. Oceanogr.*, *37*, 2740–2763, doi:10.1175/2007JPO3586.1.

Eriksen, C. C. (1985), Implication of ocean bottom reflection for internal wave spectra and mixing, *J. Phys. Oceanogr.*, *15*, 1145–1156, doi:10.1175/1520-0485(1985)015<1145:IOOBRF>2.0.CO;2.

Farmer, M. D., and L. Armi (1999a), The generation and trapping of solitary waves over topography, *Science*, *283*(5399), 188–190, doi:10.1126/science.283.5399.188.

Farmer, M. D., and L. Armi (1999b), Stratified flow over topography: Role of small scale entrainment and mixing, *Proc. R. Soc. London*, *455*, 3221–3258, doi:10.1098/rspa.1999.0448.

Farmer, M. D., and S. J. Dugan (1980), Tidal interaction of stratified flow with a sill in Knight Inlet, *Deep Sea Res.*, *27*, 239–254, doi:10.1016/0198-0149(80)90015-1.

Hall, P., and A. M. Davies (2005), Effect of coastal boundary resolution and mixing upon internal wave generation and propagation in coastal regions, *Ocean Dyn.*, *55*, 248–271, doi:10.1007/s10236-005-0014-5.

Holt, J. T., and S. A. Thorpe (1997), The propagation of high frequency internal waves in the Celtic Sea, *Deep Sea Res., Part I*, *44*, 2087–2116, doi:10.1016/S0967-0637(97)00091-5.

Inall, M. E., F. R. Cottier, C. Griffiths, and T. P. Rippeth (2004), Sill dynamics and energy transformation in a jet fjord, *Ocean Dyn.*, *54*, 307–314, doi:10.1007/s10236-003-0059-2.

Inall, M. E., T. P. Rippeth, C. Griffiths, and P. Wiles (2005), Evolution and distribution of TKE production and dissipation within stratified flow over topography, *Geophys. Res. Lett.*, *32*, L08607, doi:10.1029/2004GL022289.

Johnsson, M., J. A. M. Green, and A. Stigebrandt (2007), Baroclinic wave drag from two closely spaced sills in a narrow fjord as inferred from basin water mixing, *J. Geophys. Res.*, *112*, C11002, doi:10.1029/2006JC003694.

Klymak, J. M., and S. M. Legg (2010), A simple mixing scheme for models that resolve breaking internal waves, *Ocean Modell.*, *33*, 224–234, doi:10.1016/j.ocemod.2010.02.005.

Klymak, J. M., S. M. Legg, and R. Pinkel (2010), High-mode stationary waves in stratified flow over large obstacles, *J. Fluid Mech.*, *644*, 321–336, doi:10.1017/S0022112009992503.

Lamb, K. G. (1994), Numerical experiments of internal wave generation by strong tidal flow across a finite amplitude bank edge, *J. Geophys. Res.*, *99*, 843–864, doi:10.1029/93JC02514.

Lamb, K. G. (2004), Nonlinear interaction among internal wave beams generated by tidal flow over supercritical topography, *Geophys. Res. Lett.*, *31*, L09313, doi:10.1029/2003GL019393.

Legg, S. (2004a), Internal tides generated on a corrugated continental slope. Part I: Cross slope barotropic forcing, *J. Phys. Oceanogr.*, *34*, 156–173, doi:10.1175/1520-0485(2004)034<0156:ITGOAC>2.0.CO;2.

Legg, S. (2004b), Internal tides generated on a corrugated continental slope. Part II: Along-slope barotropic forcing, *J. Phys. Oceanogr.*, *34*, 1824–1838, doi:10.1175/1520-0485(2004)034<1824:ITGOAC>2.0.CO;2.

Legg, S., and K. M. H. Huijts (2006), Preliminary simulations of internal waves and mixing generated by finite amplitude tidal flow over isolated topography, *Deep Sea Res., Part II*, *53*, 140–156, doi:10.1016/j.dsr2.2005.09.014.

Legg, S. M., and J. M. Klymak (2008), Internal hydraulic jumps and overturning generated by tidal flow over a tall steep ridge, *J. Phys. Oceanogr.*, *38*, 1949–1964, doi:10.1175/2008JPO3777.1.

Maas, L. R. M., and F.-P. A. Lam (1995), Geometric focusing of internal waves, *J. Fluid Mech.*, *300*, 1–41, doi:10.1017/S0022112095003582.

Marshall, J., C. Hill, L. Perelman, and A. Adcroft (1997), Hydrostatic, quasi-hydrostatic and nonhydrostatic ocean modelling, *J. Geophys. Res.*, *102*, 5733–5752, doi:10.1029/96JC02776.

Moum, J. N., J. M. Klymak, J. D. Nash, A. Perlin, and W. D. Smyth (2007), Energy transport by non-linear internal waves, *J. Phys. Oceanogr.*, *37*, 1968–1988, doi:10.1175/JPO3094.1.

Nakamura, T., and T. Awaji (2001), A growth mechanism for topographic internal waves generated by an oscillatory flow, *J. Phys. Oceanogr.*, *31*, 2511–2524, doi:10.1175/1520-0485(2001)031<2511:AGMFTI>2.0.CO;2.

Nakamura, T., T. Awaji, T. Hatayama, and K. Akitomo (2000), The generation of large-amplitude unsteady lee waves by sub-inertial K_1 tidal flow: A possible vertical mixing mechanism in the Kuril Straits, *J. Phys. Oceanogr.*, *30*, 1601–1621, doi:10.1175/1520-0485(2000)030<1601:TGOLAU>2.0.CO;2.

Nycander, J. (2005), Generation of internal waves in the deep ocean by tides, *J. Geophys. Res.*, *110*, C10028, doi:10.1029/2004JC002487.

Nycander, J. (2006), Tidal generation of internal waves from a periodic array of steep ridges, *J. Fluid Mech.*, *567*, 415–432, doi:10.1017/S002211200600228X.

Petruncio, E. T., L. K. Rosenfeld, and J. D. Paduan (1998), Observations of the internal tide in Monterey Canyon, *J. Phys. Oceanogr.*, *28*, 1873–1903, doi:10.1175/1520-0485(1998)028<1873:OOTITI>2.0.CO;2.

Pingree, R. D., and A. L. New (1989), Downward propagation of internal tidal energy into the Bay of Biscay, *Deep Sea Res.*, *36*, 735–758, doi:10.1016/0198-0149(89)90148-9.

Pingree, R. D., and A. L. New (1991), Abyssal penetration and bottom reflection of internal tide energy into the Bay of Biscay, *J. Phys. Oceanogr.*, *21*, 28–39, doi:10.1175/1520-0485(1991)021<0028:APABRO>2.0.CO;2.

Rennau, H., and H. Burchard (2009), Quantitative analysis of numerically induced mixing in a coastal model application, *Ocean Dyn.*, *59*, 671–687, doi:10.1007/s10236-009-0201-x.

Saenko, O. A. (2006), The effect of localized mixing on the ocean circulation and time-dependent climate change, *J. Phys. Oceanogr.*, *36*, 140–160, doi:10.1175/JPO2839.1.

Samelson, R. M. (1998), Large scale circulation with locally enhanced vertical mixing, *J. Phys. Oceanogr.*, *28*, 712–726, doi:10.1175/1520-0485(1998)028<0712:LSCWLE>2.0.CO;2.

Spall, M. A. (2001), Large scale circulations forced by localized mixing over a sloping bottom, *J. Phys. Oceanogr.*, *31*, 2369–2384, doi:10.1175/1520-0485(2001)031<2369:LSCFBL>2.0.CO;2.

Thorpe, S. A. (2001), Internal wave reflection and scattering from sloping rough topography, *J. Phys. Oceanogr.*, *31*, 537–553, doi:10.1175/1520-0485(2001)031<0537:IWRASF>2.0.CO;2.

Van Haren, H. (2004), Some observations of non-linearly modified internal wave spectra, *J. Geophys. Res.*, *109*, C03045, doi:10.1029/2003JC002136.

Van Haren, H., L. Maas, and H. Van Aken (2002) On the nature of internal wave spectra near a continental slope, *Geophys. Res. Lett.*, *29*(12), 1615, doi:10.1029/2001GL014341.

Venayagamoorthy, S. K., and O. B. Fringer (2005), Nonhydrostatic and nonlinear contributions to the energy flux budget in non-linear internal waves, *Geophys. Res. Lett.*, *32*, L15603, doi:10.1029/2005GL023432.

Vlasenko, V., N. Stashchuk, and K. Hutter (2002), Water exchange in fjords induced by tidally generated internal lee waves, *Dyn. Atmos. Oceans*, *35*, 63–89, doi:10.1016/S0377-0265(01)00085-9.

Vlasenko, V., N. Stashchuk, and K. Hutter (2005), *Baroclinic Tides: Theoretical Modelling and Observational Evidence*, Cambridge Univ. Press, New York, doi:10.1017/CBO9780511535932.

Xing, J., and A. M. Davies (1998), A three-dimensional model of internal tides on the Malin-Hebrides shelf and shelf edge, *J. Geophys. Res.*, *103*, 27,821–27,847, doi:10.1029/98JC02149.

Xing, J., and A. M. Davies (2006) Influence of stratification and topography upon internal wave spectra in the region of sills, *Geophys. Res. Lett.*, *33*, L23606, doi:10.1029/2006GL028092.

Xing, J., and A. M. Davies (2007), On the importance of non-hydrostatic processes in determining tidally induced mixing in sill regions, *Cont. Shelf Res.*, *27*, 2162–2185, doi:10.1016/j.csr.2007.05.012.

Xing, J., and A. M. Davies (2009) Influence of multiple sills upon internal wave generation and implications for mixing, *Geophys. Res. Lett.*, *36*, L13602, doi:10.1029/2009GL038181.

A. M. Davies and J. Xing, National Oceanography Centre, 6 Brownlow St., Liverpool L3 5DA, UK. (jxx@pol.ac.uk)